

如图 3-23、3-24、3-25 所示为 800℃、750℃、700℃下 Ce111 和 Ce113 的 SOEC 模式下的 IV 曲线对比。700℃、750℃条件下, 1.3V 的两者电流密度十分接近, Ce111 电流密度略大于 Ce113。当温度上升到 800℃时, Ce111、Ce113 在 1.3V 时电流密度分别为 $7.12 \text{ mA} \cdot \text{cm}^{-2}$ 、 $6.21 \text{ mA} \cdot \text{cm}^{-2}$, CO 生成速率 $2.976 \text{ mLh}^{-1} \text{cm}^{-2}$ 和 $2.6 \text{ mLh}^{-1} \text{cm}^{-2}$, Ce111 在该温度下电解 CO₂ 性能优于 Ce112。

4 总结

4 Conclusions

本文采用压片法的方法分别制作了以镧锶锰氧 (LSM) 为氧气极材料电解质支撑性电池 (Ce113) 以及镧锶钴铁 (LSCF) (Ce111) 为氧气极材料电解质支撑性电池。将制备好的 Ce111 和 Ce113 连同镧锶锰氧 (LSM) 为氧气极材料燃料极支撑性电池 (Ce112) 进行了电化学阻抗谱 (EIS) 的测试、固体氧化物燃料电池 SOFC 模式下的 I-V、I-P 曲线测试和固体氧化物电解池 SOEC 模式下的 I-V 曲线测试, 并对测试结果进行整理和对比, 得到以下几点主要结论:

(1) 固体氧化物化学池 (SOC) 的性能与工作温度相关, 实验表明工作温度越高, 三种 SOC 的总阻抗均会下降, 尤其是极化阻抗下降很快, 同时高温下的 SOFC 模式和 SOEC 模式的电流密度也会增加, SOFC 模式下消耗 H_2 释放电能和 SOEC 模式下电解 CO_2 释放 CO 的速率也会更快。

(2) 通过的压片法制备的 Ce111 和 Ce113 电池是电解质支撑性的电池, 相比与通过流延法制备得到的 Ce112 电池, 电解质层厚度很大很, 电阻会明显地增大, 本实验中 $800^\circ C$ 时, Ce112 的总阻抗仅为 $1.87 \Omega cm^2$, 而 Ce111 和 Ce113 的总阻抗达到了 $40.93 \Omega cm^2$ 、 $28.8 \Omega cm^2$ 。过大的总阻抗极大地影响了电池在 SOFC 模式下放电和 SOEC 模式下电解性能。同时, 在本实验中由于 Ce112 电池的电解质层过于薄而出现电解质层没有形成致密的一层而导致在 SOFC 模式和 SOEC 模式下开路电压 (OCV) 低于理论值, 表明流延法制备的电池工艺相对困难。所以, 优良的电池电解质层要越薄总阻抗越小越好, 同时要保证电解质层致密。

(3) 同为电解质支撑性的 Ce111 和 Ce113 电池在电化学阻抗谱 (EIS) 上, 两者的欧姆阻抗接近, 但是 LSM 为燃料极材料的 Ce113 电池的极化阻抗明显比 LSCF 为燃料极材料的 Ce111 电池的极化阻抗要小。在以 H_2 为燃料的 SOFC 模式中的 I-V 曲线图, 两者在 $700^\circ C$ 、 $750^\circ C$ 时性能相当, Ce111 的同电压电流密度略大性能会略好些, $800^\circ C$ 时, Ce111 的性能明显好于 Ce113。以 CO_2 为电解气体的 SOEC 的 I-V 曲线上, $700^\circ C$ 、 $750^\circ C$ 时外加电压为 1.3V 的 Ce111 的 CO 生成速率分别 $0.819 mLh^{-1}cm^{-2}$ 和 $1.371 mLh^{-1}cm^{-2}$, Ce113 在 $700^\circ C$ 、 $750^\circ C$ 外加电压为 1.3V 的时 CO 生成速率为 $1.47 mLh^{-1}cm^{-2}$ 、 $1.04 mLh^{-1}cm^{-2}$, 两者差异不大。 $800^\circ C$ 时, 外加 1.3V 电压的 Ce111 的 CO 生成速率 $2.976 mLh^{-1}cm^{-2}$, Ce113 的 CO 生成速率为 $2.60 mLh^{-1}cm^{-2}$, 总体来说 $700^\circ C$ 和 $750^\circ C$ 时, 两者的 SOC 性能差异不大。 $800^\circ C$ 时以 LSCF 为氧气极材料的电池比 LSM 为氧气极材料的 SOC 性能更优

参考文献

- [1]. 刘仁柱, 阳极支撑型管式固体氧化物燃料电池的制备与优化[D]. 上海: 中国科学院上海硅酸盐研究所, 2010, 23-24.
- [2]. EIA. How much of our electricity is generated from renewable energy? [OL]. [2013-4-22] http://www.eia.gov/energy_in_brief/article/renewable_electricity.cfm.
- [3]. 中国可再生能源学会光伏专业委员会. 光伏年装机调至 1000 万千瓦. 能源工作会议力推新能源 [OL]. [2013-1-9].
- [4]. 中国风能协会. 2012 年我国风电装机容量达到 1404.9 万千瓦 [OL]. [2013-2-5] http://www.cwea.org.cn/hynews/display_info.asp?cid=364.
- [5]. Liu J. Direct-hydrocarbon solid oxide fuel cells [J]. Progress in Chemistry, 2006, 18 (7): 1026-1059.
- [6]. 张文亮, 丘明, 来小康. 储能技术在电力系统中的应用[J]. 电网技术, 2008, 32(7): 1-9.
- [7]. 中国科学院过程工程研究所. 不密封无联接极固体氧化物燃料电池发电成功[J]. 电源技术应用. 2007, 04: 40.
- [8]. Ni M, Leung MKH, Sumathy K, Leung DYC. Potential of renewable hydrogen production for energy supply in Hong Kong [J]. Int J Hydrogen Energy, 2006; 31:1401–1413.
- [9]. Ni M, Leung MKH, Sumathy K, Leung DYC, Sumathy K. A review and recent developments in photocatalytic water-splitting using TiO₂ for hydrogen production. Renewable Sustainable Energy Rev [J], Int. J. Hydrogen Energy, 2007, 11 (3): 401–426.
- [10]. Shin, Y., W. Park, Chang, J.H. Park, J. Evaluation of the high temperature electrolysis of steam to produce hydrogen [J]. Int J Hydrogen Energy, 2006; 32:1486-1577.
- [11]. Briss A., Schefold J., Zahid M. High temperature water electrolysis in solid oxide cells [J]. Int. J. Hydrogen Energy, 2008; 33:5375-5457.
- [12]. Ni M, Leung MKH, Sumathy K, Leung DYC. Technological development of hydrogen production by solid oxide electrolyzer cell (SOEC) [J]. Int. J. Hydrogen Energy, 2008; 33: 2337-2391.
- [13]. Fujiwara S, Kasai S, Yamauchi H, Yamada K., Makino S, Matsuyama K, Yoshino M, Kameda T, Ogawa T, Momma S, Hoashi E. Hydrogen production by high temperature electrolysis with nuclear reactor [J]. Progress in Nuclear Energy, 2008(50): 422-426.
- [14]. 李建林, 许洪华, 高志刚. 风力发电中的电力电子变流技术[M]. 北京: 机械工业出版社, 2008.
- [15]. 李松丽, 王绍荣, 曹佳弟, 聂怀文, 温廷璁. 浸渍成型管式固体氧化物燃料电池的方法. 中国: 200510026299.9 [P]. 2005.11.23.
- [16]. Hauch A., S. D Ebbesen, M Mogensen. Highly efficient high temperature electrolysis [J] J.

Mater. Chem. 2008; 18:2331-2371.

[17]. 王景儒. 制氢方法及储氢材料研制进展 [J]. 化学推进剂与高分子材料, 2004, 4(2):13-17.

[18]. Holladay J D, Hu J, King D L, Wang Y. An overview of hydrogen production technologies [J]. Catalysis Today, 2009(139): 244-260.

[19]. H. Song, L. Zhang, R.B. Watson, D. Braden, U.S. Ozkan, Investigation of bio-ethanol steam reforming over cobalt-based catalysts [J]. Catalysis Today, 2007,129 (3-4): 346-354.

[20]. Meyer S, Hsing C. Modern and prospective technologies for hydrogen production from fossil fuels [J]. Int. J. Hydrogen Energy, 1989, 14: 797~ 820.

[21]. 傅献彩, 沈文霞, 姚天扬, 侯文华. 物理化学[M]. 北京: 高等教育出版社, 2006.

[22]. Weikang Hu, Xuejun Cao, Fupeng Wang, Yunshi Zhang. A Novel Cathode For Alkaline Water Electrolysis [J] Int. J. Hydrogen Energy, 1997, 22: 441-443.

[23]. G Schiller, R Henne, P Mohr, V. Peinecke, High Performance Electrodes For An Advanced Intermittently Operated 10 kW Alkaline Water Electrolyzer [J] Int. J. Hydrogen Energy, 1998, 23: 761-765.

[24]. P Millet, F Andolfatto, R Durand, Design and Performance of a Solid Polymer Electrolyte Water Electrolyzer [J]. Int. J. Hydrogen Energy, 1996, 21: 87-93.

[25]. Egil Rasten, Georg Hagen, Reidar Tunold. Electrocatalysis in Water Electrolysis with Solid Polymer Electrolyzer [J]. Electrochimica Acta, 2003, 48: 3945-3952.

[26]. Friberg, R. A photovoltaic solar-hydrogen power plant for rural electrification in India. Part 1: a general survey of technologies applicable within the solar-hydrogen concept [J]. Int. J. Hydrogen Energy, 1993, 18: 853-882.

[27]. Turner J, Sverdrup G, Mann M K., Maness P C, Kroposki B, Ghirardi M, Evans R J, Blake D. Renewable hydrogen production [J]. International Journal of Energy Research, 2008, 32: 379-407.

[28]. Chum H L, Overend R P, Biomass and renewable fuels [J]. Fuel Processing Technology, 2001, 71: 187-195.

[29]. Demirbas A. Combustion characteristics of different biomass fuels [J]. Progress in Energy and Combustion Science, 2004, 30: 219-230.

[30]. Hino R, Haga K, Aita H, Sekita, K. R&D on hydrogen production by high-temperature electrolysis of steam [J]. Nuclear Engineering and Design, 2004, 233: 363-375.

[31]. Knibbe R, Traulsen M L, Hauch A, Ebbesen S D, Mogensen M. Solid Oxide Electrolysis Cells: Degradation at High Current Densities [J]. Journal of the Electrochemical Society, 2010, 157: B1209-B1217.

[32]. 刘明义, 于波, 徐景明. 固体氧化物电解水制氢系统效率. 清华大学学报(自然科学版)

2009, 49 (6): 20-34.

[33]. Singhal S C. Advances in solid oxide fuel cell technology [J], Solid State Ionics, 2000 ,135: 305-313.

[34]. Kabs H. Advanced SOFC technology and its Realization at Siemens Westinghouse [R], Bilateral Seminars 33, Materials and processes for Advanced Technology: Materials for Energy systems, Egyptian-German Workshop, Cairo, 7-9 April 2002, Eds. D. Stover and M. Bram, Julich Germany, 2002: 91-101.

[35]. 周利, 程谟杰, 衣宝廉. 管型固体氧化物燃料电池技术进展[J]. 电池, 2005, 35 (1): 63-65.

[36]. Vora S D. Development of high power density seal-less SOFCs [J]. ECS Transactions, 2007, 7(1): 149-154.

[37]. Diguiuseppe G. High power density cell development at Siemens Westinghouse [A]. 9th Symposium on Solid Oxide Fuel Cells (SOFC-IX) [C], Quebec, Canada, 2005: 322-332.

[38]. Vora S D. Development of high power density seal-less SOFCs [A]. International Symposium on Solid Oxide Fuel Cells (SOFC-X) [C], Nara, Japan, 2006: 9-12.

[39]. Wolf V, Arnold L, Hubert A G. Handbook of Fuel Cells [M]. New York: Wiley, 2003.

[40]. Brown M, Fenton B, Gaw K. Horizontal fuel cell tube systems and methods US, US6841284 [P]. 2005-1-11.

[41]张宇, 俞国勤, 施明融, 杨林青. 电力储能应用技术前景分析[J]. 华东电力, 2008, 36(4): 92-93.

[42]. Jing Sui, Jiang Liu. Slip-Cast $\text{Ce}_{0.8}\text{Sm}_{0.2}\text{O}_{1.9}$ Cone-Shaped SOFC [J]. J. Am. Ceram. SOC, 2008, 91 (4):1335-1337.

[43]. Yaohui Zhang, Jiang Liu. Fabrication and performance of Cone-shaped Segmented-In-Series Solid Oxide Fuel Cells[J]. J. Appl. Ceram Technology, 2008, 5(6): 568-573.

[44]. Tinglian Wen. Research on planar SOFC stacks [J]. Solid State Ionics, 2002, 152:399-404.

[45]. Wilchens R S, Hartr L G J D, Vinke I C, Blum L. Recent results stack development at Forschungszentrum Julich, Fuel Cell Technologies: State and perspectives [M]. Springer Netherlands, 2005, 202: 123-134.

[46]. Bujalski W, Dikwal C M, Kendall K. Cycling of three solid oxide fuel cell types [J]. J Power Sources, 2007, 171: 96-100.

[47]. Brandon N P. Materials engineering for solid oxide fuel cell technology [J]. Mater Sci Forum, 2007, 539: 20-27.

[48]. 施剑林. 现代无机非金属材料工艺学[M]. 长春: 吉林科学技术出版社, 1993.

[49]. Singhal S C. Science and Technology of Solid-Oxide Fuel Cells [J]. MRS Bulletin, 2000, 25.

- [50]. 蔡祖光. 陶瓷辊棒的螺旋的挤出成型[J]. 现代技术陶瓷, 2002, 3:31-33.
- [51]. 刘学建, 黄莉萍, 古宏晨, 符锡仁. 陶瓷成型方法研究进展 [J]. 陶瓷学报, 1999, 20 (4): 230-234.
- [52] Rao R, Roopa H N, Kannan T S. The characterization of aqueous silicon slips [J]. Journal of the European Ceramic Society, 1999, 19: 2763-2771.
- [53]. 刘康时. 陶瓷工艺学[M]. 北京: 中国建筑工业出版社, 1981.
- [54]. Zhang L, He H Q, Kwek W R, Ma J, Tang E H, Jiang S P. Fabrication and Characterization of Anode-Supported Tubular Solid-Oxide Fuel Cells by Slip Casting and Dip Coating Techniques [J]. Journal of the American Ceramic Society, 2009, 92: 302-310.
- [55]. Li S, Wang S, Nie H., Wen T. A direct-methane solid oxide fuel cell with a double-layer anode [J]. Journal of Solid State Electrochemistry, 2007, 11: 59-64.
- [56]. 郑积渊. 跨世纪科技与社会可持续发展[M]. 北京: 人民出版社, 1998.

翻译部分

英文原文

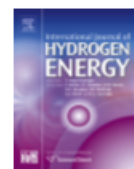
INTERNATIONAL JOURNAL OF HYDROGEN ENERGY 41 (2016) 17233–17246



Available online at www.sciencedirect.com

ScienceDirect

journal homepage: www.elsevier.com/locate/he



Operating maps of high temperature H₂O electrolysis and H₂O+CO₂ co-electrolysis in solid oxide cells

J. Aicart ^{a,b}, F. Usseglio-Viretta ^a, J. Laurencin ^{a,*}, M. Petitjean ^a,
G. Delette ^a, L. Dessemond ^b

^a Univ. Grenoble Alpes – CEA, LITEN, 17 rue des Martyrs, F-38054 Grenoble, France

^b Univ. Grenoble Alpes – CNRS, Laboratoire d'Electrochimie et de Physicochimie des Matériaux et des Interfaces, F-38000 Grenoble, France

ARTICLE INFO

Article history:

Received 12 May 2016

Received in revised form

11 July 2016

Accepted 31 July 2016

Available online 24 August 2016

Keywords:

Solid oxide cell

Steam electrolysis

H₂O CO₂ co-electrolysis

Modeling

Operating map

ABSTRACT

This work aims at investigating through a modeling approach the difference in thermal and electrochemical responses between high temperature H₂O electrolysis and H₂O+CO₂ co-electrolysis in solid oxide cells. The study has been conducted by considering a typical planar stack configuration with cathode supported cells. The influence of the local temperature on the polarization curve is discussed. Operating maps are simulated for both electrolysis modes depending on cell voltage and inlet gas flow rate, covering a complete range of gas conversion rates. The optimum domains of operating conditions combining high performances and reasonable temperature elevations are identified. In overall, higher performances are found in steam electrolysis. Indeed, the co-electrolysis process is found to be strongly limited by mass transport through the thick cathode. However, co-electrolysis exhibits an easier thermal management. Finally, the composition of the syn-gas produced by co-electrolysis is found to be highly flexible through adjustments of the operating parameters.

© 2016 Hydrogen Energy Publications LLC. Published by Elsevier Ltd. All rights reserved.

Introduction

Because of the expected fossil fuel depletion and the raising public awareness of environmental pressures, the current oil/natural gas/coal-based energy conversion system must be shifted towards renewable energy sources with low carbon footprint. However, because storing electricity over an extended period of time remains a challenge, this transition must rely on suitable energy carriers. Due to its high energy content and potentially nil carbon impact, hydrogen,

associated with electrochemical converters, could play a significant role in the near future.

Nowadays, high temperature steam electrolysis (HTSE) – chemical reaction (1) – based on solid oxide cells (SOCs) has become a major subject of investigations. This promising technology is able to produce H₂ at a low electrical cost since a part of the required energy for water splitting is supplied by heat. Consequently, the electrical-to-chemical efficiency of HTSE at 800 °C has been shown to reach very high values, especially if the SOC is supplied with waste heat [1].

* Corresponding author. Fax: +33 4 38784139.

E-mail address: jerome.laurencin@cea.fr (J. Laurencin).

<http://dx.doi.org/10.1016/j.ijhydene.2016.07.269>

0360-3199/© 2016 Hydrogen Energy Publications LLC. Published by Elsevier Ltd. All rights reserved.

Furthermore, thanks to the high operating temperature, SOCs offer the ability to electrolyze CO_2 to produce CO (2) [2–5], and co-electrolyze H_2O and CO_2 to yield H_2 +CO syngas (3). In this last operating mode, the water gas shift (WGS) reaction (4) also occurs and participates to the global process of CO generation. Since easily storable end products – such as methane, methanol synthetic petroleum, gasoline, etc. – can be produced from syngas, co-electrolysis could be of high interest in any scenario where electricity is stored under the form of a fuel (i.e. usually named Power-to-Gas or Power-to-Liquid). Indeed, the complete route, (i) atmospheric CO_2 capture using solid sorbent, (ii) H_2O + CO_2 co-electrolysis and (iii) synthetic fuel production based on the Fischer-Tropsch process [6,7], was identified as one of the most energy efficient and economically viable Power-to-Fuel paths [8]. Though fuel price, O_2 product value and CO_2 cost can be limiting factors [9], the potential of Power-to-Gas/Liquid processes is being assessed worldwide through numerous on-going research programs [10]. Eventually, both high temperature H_2O and H_2O + CO_2 electrolysis processes could produce efficient energy carriers, enabling massive implementation of renewable energy sources disconnected from power grids.



Nevertheless, to become economically viable, it is still needed to improve the performances, durability and reliability of SOCs altogether [11]. In that objective, various experimental studies have been devoted to assess the SOCs electrochemical response in operation. It was shown that similar performances can be obtained in both steam and co-electrolysis for specific operating conditions [2,12,13]. In addition, again for specific operating conditions, both electrolysis modes usually display rather comparable degradation rates [13–16]. Indeed, the most likely underlying mechanisms inducing the cell aging could be independent of the electrolysis operating modes. For instance, it was shown that cell degradation could be mainly due to Ni particles coarsening driven by the temperature [17], impurities present in the inlet gases [18], and/or to oxygen pressure build-up [19]. However, even if SOC durability still needs to be improved, the high performances of both H_2O and H_2O + CO_2 electrolysis processes have been demonstrated at the button cell and the stack levels [20–26]. These promising results have recently triggered tremendous efforts to scale-up the high temperature electrolysis and co-electrolysis technologies [15,22,27–30]. However, to efficiently operate large active area stacks (i.e. pileup of single repeating units – SRUs –, each containing one SOC), a better understanding of thermal phenomena, and their influence on performances and outlet compositions, is still required. For this purpose, the modeling tool can constitute an efficient approach to analyze the impact on performances of all the coupled mass and energy transfers occurring within the single repeating unit SRU or stack.

At the SOC/stack scale, several models, with different levels of complexity, have recently been developed to investigate HTSE [31–38] or co-electrolysis [14,27,39–46] processes. Concerning syngas production, two main assumptions have been considered in the modeling approaches. The first is based on CO being solely produced through the reverse WGS reaction [14,27,38]. The second one considers that both CO_2 electrolysis and the WGS reaction are liable to generate CO [39,43–45]. In the latter case, it was shown that the relative direction of the WGS reaction could be dependent both on the inlet composition and on the location within the electrochemical cell [39,44]. It should be noted that the relative influence of the reverse WGS over CO production is likely to be current dependent. At low current densities, the kinetics of the chemical reaction are fast enough so that CO production through electrochemical reduction of CO_2 can accurately be neglected [14,47]. At higher co-electrolysis current density, CO electrochemical production may become preponderant [24].

In previous works, complete 2D in-house-models were developed at the SRU or stack level to simulate both H_2O electrolysis [48] and co-electrolysis [44]. A macroscopic representation of the co-electrolysis mechanism was introduced [43], and experimentally validated [24,44]. These studies were mainly based on single SOCs operated in isothermal conditions at $T = 800^\circ\text{C}$. However, the cell thermal management in a stack environment is a key issue that can potentially lead to very high temperature elevation or cooling depending on the operating voltage [48]. These temperature changes can significantly affect the cells response and are accompanied by strong thermal gradients along the cell. Because of the mismatch in thermal expansions between the cell layers, these gradients can induce mechanical damage such as delamination [49,50] and electrode [51] or electrolyte cracking [49].

The present work aims at establishing H_2O electrolysis and H_2O + CO_2 co-electrolysis operating maps through a modeling approach. The simulations are analyzed in order to determine optimized practical operating conditions. Accordingly, the geometry of a typical planar SRU, representative of a stack, is investigated. In addition, the influence of local temperatures on performances is considered. This approach should provide useful insights towards evaluating further the technological relevance of high temperature electrolysis processes. Indeed, although some parametric studies exist concerning isothermal HTSE [52] or co-electrolysis economic assessment [9], to the best of the authors' knowledge, operating maps accounting for the coupling between thermal and electrochemical phenomena have not been investigated yet.

Modeling approach

Both the steam electrolysis and co-electrolysis models are exhaustively described elsewhere [21,44,48]. However, this section strives to summarize the main model assumptions, experimental validations, and to describe the geometry and materials investigated.

Hypotheses and experimental validations

The global model architecture is composed of an integrated mass transfer and electrochemical module coupled to a thermal one. The thermal calculations were solved within the frame of the finite elements code Cast3M [53], while the electrochemical module was implemented using the commercial software Matlab®. The following sections focus on the description of the co-electrolysis model, due to its enhanced complexity stemming from additional gas species. Nevertheless, the steam electrolysis model can be deduced from the following if no CO₂ nor CO are fed to the cell.

Electrochemical module

The proposed co-electrolysis model describes the H₂ and CO production through electroreduction reactions of steam (5) and carbon dioxide (6), occurring simultaneously at the cathode side, while oxygen is produced at the anode side (7). The WGS reaction (4) is assumed to occur in the pores of the cathode material. Considering a SOC operating at high temperature and atmospheric pressure, carbon deposition and methane production have been neglected [24,41,54,55].



Electrochemical kinetics are described through a generalized Butler–Volmer equation. The cell voltage U_{cell} is thus decomposed into Equation (8), which is the sum of the standard potential $U_{\text{e-o}}$, the ohmic losses, and the overpotentials for activation and concentration, η_{act} and η_{conc} respectively.

$$U_{\text{cell}} = U_{\text{e-o}} + R_{\text{ohm}}|i| + |\eta_{\text{act}}^{\text{anode}}| + |\eta_{\text{act}}^{\text{cathode}}| + |\eta_{\text{conc}}^{\text{anode}}| + |\eta_{\text{conc}}^{\text{cathode}}| \quad (8)$$

$$|\eta_{\text{act}}| = \frac{RT}{F} \sinh^{-1} \left(\frac{|i|}{2i_0} \right) \quad (9)$$

Concentration overpotentials describe the voltage increase both due to active species depletion/production along the cell, and to diffusion through the porous electrodes. They are computed through Nernst equation. Activation overpotentials, accounting for electrochemical kinetics, depend on exchange current densities i_0 (Equation (9)), which represent the readiness of the electrode material to proceed with the corresponding electrochemical reaction. In the present macro scale modeling approach, the electrochemically active zones are reduced to the electrode/electrolyte interfaces. The relevance of this assumption is well verified for sufficiently thick electrodes [56–58]. Consequently, exchange current densities are macroscopic parameters that include the global electrochemical process and its delocalization into the active layers [59]. Due to presence of CO₂, the active sites of the fuel electrode are potentially not fully available for the water molecules electrolysis. Accordingly, each elementary active surface of the cathode has been split into one surface related to H₂O electrolysis, β , and a second one associated to the electrochemical reduction of CO₂, $1-\beta$ [43]. Furthermore, the local active site distribution for both electrochemical

reactions is suggested to be directly given by the relative percentage of H₂O and CO₂ at the cathode/electrolyte interface [43,60] (Equation (10)):

$$\beta = \frac{y_{\text{H}_2\text{O}}^{\text{int}}}{(y_{\text{H}_2\text{O}}^{\text{int}} + y_{\text{CO}_2}^{\text{int}})} \quad (10)$$

Mass transfer in the porous electrodes is described within the frame of the Dusty Gas Model (DGM), combining the Stefan–Maxwell and Knudsen diffusion mechanisms [61]. It is driven by the flowrates of production and consumption of active species at the electrochemical interfaces. Assuming an ideal current efficiency (i.e. ionic transport number in the electrolyte equal to 1), these flowrates are linked to the current density through Faraday's law.

Thermal module

The thermal description of the SOC includes heat transfer by conduction, convection and radiation [48,62]. As the Peclet number calculated within both electrodes is much lower than unity, porous anode and cathode are modeled as a homogeneous media for which only an effective conduction is taken into account [63]. Heat transfer by convection between external surfaces of solid parts and fluids allows computing gas temperature variations into the channels of gas distribution. Finally, radiative losses arising between the SRU and the stack insulation are also taken into account in the model.

Electrochemical and thermal coupling

In a stack configuration, the temperature evolution under polarization can greatly impact the performances, while the thermal gradients can potentially affect the SOEC structural integrity [51]. Thus, a special attention has been paid in the present work to assess the influence of local temperature variations on the cell response. For this purpose, the thermal module is intimately coupled to the electrochemical one:

(1) The generation of heat sources or sinks is computed in the electrochemical model as a function of the chemical and electrochemical kinetics rates. These sources or sinks are used as thermal loadings for the temperature computations. They are spatially distributed in the electrodes according to both (i) the repartition of the WGS reaction rates within the cathode and (ii) the evolutions of the electrochemical reactions rates along the interfaces with the electrolyte. Moreover, the gas composition profile within the SRU allows to express the evolutions of the thermofluids properties used in the thermal module. Effective conductivities of fluids are thus calculated for each position along the gas channel through a mixture law. The heat exchange coefficients between solid and gases at the anode and cathode sides are expressed from the effective gas conductivities, and hence, also evolves along the gas channels.

(2) Conversely, the temperature field coming from the thermal module is used as boundary condition in the electrochemical model. Indeed, temperature affects the local ionic conductivity of the electrolyte according to an Arrhenius law (whereas the electrical conductivities of electrodes are supposed to be high enough to be temperature independent). The kinetic constant of the WGS reaction and the electrode exchange current densities reflecting the electrochemical kinetics are also assumed to be thermally activated. Therefore,

exchange current densities are calculated as function of the local temperature T through an Arrhenius law (Table 1):

$$i_0(T) = i_0^0 \exp\left(-\frac{E_a}{RT}\right) \quad (11)$$

where i_0^0 is a pre-exponential factor, E_a the activation energy, R the gas constant and T the local temperature. Finally, it can be noticed that the diffusion of gaseous species exhibits a non-activated temperature dependence. Actually, the Knudsen coefficients are taken in the model proportional to the square root of the temperature [64] while the binary diffusivities exhibit a temperature dependence in $T^{1.75}$ (according to the Fuller theory [65]).

Model validation

These models have been validated, at the cell level, through multiple comparisons between experimental and simulated isothermal polarization curves obtained in H_2O electrolysis, CO_2 electrolysis and co-electrolysis [24,44]. In addition, the co-electrolysis model was shown to accurately predict outlet gas composition of a single SOC operated between OCV and -1.75 A cm^{-2} [24], as well as of a 25-cell stack [22]. Additional comparison with experimental data was performed in SOFC mode fueled with CH_4 [62]. The satisfactory agreement between experimental and simulated data have highlighted the models' ability to predict SOC's performances and outlet gaseous compositions.

Conditions of simulations representative of SRU/stack design

In this work, simulations have been performed to estimate the technological potential of high temperature electrolysis and co-electrolysis processes, through the establishment of operating maps. With this objective, a typical planar SRU geometry is investigated, integrating a $10 \times 10 \text{ cm}^2$ cell fed in a counter-flow configuration (Fig. 1). It is worth mentioning that boundary conditions used for the simulations have been assumed to be representative of a repeating unit located in the

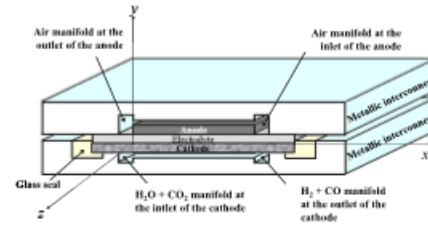


Fig. 1 – Geometry of the simulated SRU – CSC in counter-flow configuration.

middle of a complete stack. Adiabatic conditions have thus been chosen for the lower and upper surfaces of the interconnect plates, whereas the outer edges at the periphery of the simulated domain can exchange heat by radiation with the stack insulation (with a temperature maintained at $T = 800^\circ\text{C}$, see Table 1). Finally, anodic and cathodic gases are also supposed to be pre-heated to 800°C before being introduced in the stack.

The simulated cell is representative of a cathode-supported cell (CSC) configuration, which typically yields better performances than its electrolyte-supported counterpart. Most classical materials used for HTSE are considered: a Ni-8YSZ cermet as the cathode, ZrO_2 stabilized with 8 mol.% Y_2O_3 (8YSZ) as the electrolyte, and $La_{0.8}Sr_{0.2}MnO_{3-\delta}$ -8YSZ (LSM-8YSZ) as the oxygen electrode.

The cell characteristics used in the simulations are listed in Table 1. One can note that microstructural properties have been extracted from 3D electrode reconstructions obtained on a typical cell made in the same materials than the one considered for the simulations [51,59]. The pre-exponential factors of the exchange current density have been tuned to obtain typical values for the simulated electrodes (i.e. 530, 356 and 200 mA cm^{-2} for $i_{0,cathode}^{H_2-H_2O}$, $i_{0,cathode}^{CO_2-CO}$ and $i_{0,anode}$, respectively,

Table 1 – Geometric and electrochemical inputs used in the simulations. All other numerical values can be found in Refs. [48,59,62].

Single repeating unit (SRU) and cell					
Dimensions			Microstructure		
Cathode thickness	1000	μm	Tortuosity factor cathode	τ_c	2.8
Electrolyte thickness	10	μm	Porosity cathode	ϵ_c	0.43
Anode thickness	50	μm	Mean grain diameter cathode	τ_c	1.2
Cell total length	118	mm	Tortuosity factor anode	τ_a	4
Cell active length	100	mm	Porosity anode	ϵ_a	0.5
Interconnect plate thickness	10	mm	Mean grain diameter anode	τ_a	1
Gas channel width	1	mm	Furnace temperature	T_g	800 $^\circ\text{C}$
Electrochemical and electrical parameters					
$i_{H_2-H_2O}^0$	120 [51]	kJ mol^{-1}	$i_{H_2-H_2O}^0(800^\circ\text{C})$	536 [51]	mA cm^{-2}
$i_{CO_2-CO}^0$	120 [52]	kJ mol^{-1}	$i_{CO_2-CO}^0(800^\circ\text{C})$	356 ^a	mA cm^{-2}
i_{anode}^0	190 [51]	kJ mol^{-1}	$i_{anode}^0(800^\circ\text{C})$	200	mA cm^{-2}
$R_{contact}$	0.05 $\Omega \text{ cm}^2$				

^a $R_0 = i_{H_2-H_2O}^0 / i_{CO_2-CO}^0 = 1.51$ [21,44].

at 800 °C [44,59]; see Table 1). The contact resistance of the electrode/interconnect junction has been taken to a relatively low value of 0.05 Ω cm² corresponding to an optimized stack and cell.

The cathodic inlet gas composition considered for co-electrolysis investigations is given in Table 2. It has been chosen so that it should lead to the production of a syngas with a ratio of H₂/CO \approx 3/1. Indeed, that ratio constitutes a suitable composition for further conversion into synthetic methane by chemical processes [6].

Regarding H₂O electrolysis simulations, the inlet composition has been taken to 90/10 vol.% H₂O/H₂. It can be noticed that both investigated compositions for electrolysis and co-electrolysis contain the same proportion of oxidized species at the inlet. In that condition, the global conversion rates at given flow rate and current density will be identical so that the performances can be directly compared. In both electrolysis modes, the oxygen electrode has been assumed to be fed with air. As detailed in Table 2, a wide range of flowrates has been examined, from 12 to 48 Nml min⁻¹ cm⁻² in co-electrolysis mode, and from 20 to 95 Nml min⁻¹ cm⁻² in HTSE mode.

Results and discussion

Element of experimental validation

In addition to the already published model validations (cf. Section Hypotheses and experimental validations), the performances computed in the present work have been favorably compared to the ones obtained with a short stack tested at the laboratory in the same operating condition of gas feeding and temperature.

Based on the hypotheses and parameters gathered in Table 1, the simulations assess a current density of about -0.8 A cm⁻² at 1.2 V (cathodic flow: 15 Nml min⁻¹ cm⁻² of 90/10 vol.% H₂O/H₂, temperature of 800 °C used as boundary condition). In similar operating conditions, a current of -1 A cm⁻² at 1.2 V has been measured on a CSC Ni-YSZ/YSZ/LSCF-YDC 3-cell stack with an active area of 100 cm² per cell (90/10 vol.% H₂O/H₂, 15 Nml min⁻¹ cm⁻², gas preheated to 800 °C and stack insulation regulated to 800 °C) [66,67]. It is worth underlying that the present comparison between simulations and experiments is only indicative since both approaches do not consider the same cell. Consequently, the slight difference between experimental and simulated current densities is likely to arise from the difference in air electrode materials, with LSCF usually displaying higher activity (i.e. higher exchange current density) compared to LSM. Nevertheless, the calculated and measured current densities are

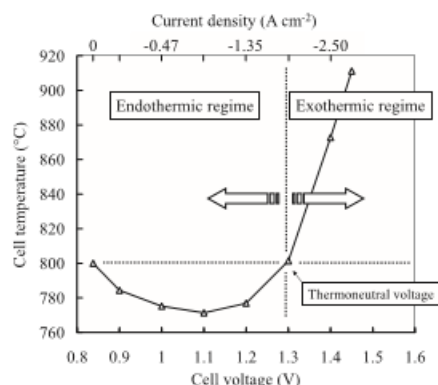


Fig. 2 – Temperature taken in the middle of the cell plotted as a function of the polarization when the SOC is operated in H₂O electrolysis mode (inlet composition corresponding to simulation A1 – Table 2).

roughly in the same order, meaning that the results obtained by simulation are representative of the performances of a real object.

Influence of the temperature on performances

The influence of polarization on the stack thermal and electrochemical responses has been studied in H₂O electrolysis (for composition A1, Table 2). In Fig. 2, the temperature in the central part of the SRU has been plotted as a function of the cell voltage. At OCV, as no current flows through the SRU, the temperature is equal to the one taken as boundary condition (i.e. T = 800 °C corresponding to the temperature of gas inlet and stack insulation). However, when the polarization increases, a strong evolution is evidenced with three thermal modes: endothermic, autothermic and exothermic modes. When the cell voltage is equal to the thermoneutral voltage (i.e. 1.29 V at T = 800 °C for H₂O electrolysis), the supplied electrical power exactly balances the enthalpy of steam dissociation (corresponding to the endothermic reaction (5)). In that condition, there is no warming nor cooling and the resulting stack temperature is equal to 800 °C. For polarizations below the thermoneutral voltage, because the electrical energy does not account entirely for the requirements of the electrochemical reaction, the energy gap has to be provided by an external supply of heat. As a consequence, the cell is operated in an

Table 2 – Inlet gas flow rates and compositions considered for the electrolysis (A1–A7) and co-electrolysis (B1–B4) simulations.

Denomination		A1	A2	A3	A4	A5	A6	A7	B1	B2	B3	B4
$F_{\text{cathode}} = F_{\text{anode}}$	NmL min ⁻¹ cm ⁻²	20	31	34	48	61	75	95	12	20	31	48
Cathode	vol.%	H ₂ O/H ₂ 90/10								H ₂ O/CO ₂ /H ₂ 65/25/10		
Anode		N ₂ /O ₂ 79/21										

endothermic mode and the temperature is decreased below 800 °C (Fig. 2). For polarizations above the thermoneutral voltage, extra heat is generated and the average cell temperature rises beyond $T = 800$ °C. In the chosen conditions, the cell average temperature is found to exceed 900 °C at 1.45 V. This very high temperature constitutes a risk in terms of electrolyzer degradation that will be discussed in the next section.

These variations of temperature due to the stack thermal regimes are liable to have a significant impact on cell performances. To give some insights on these potential effects, the polarization curve computed considering the stack thermal boundary condition has been compared to the one obtained with an isothermal assumption. This last condition is typically representative of a button cell characterized in a test bench (in that case, the cell warming or cooling is mitigated by the controlled temperature imposed by the furnace). The comparison between both cases is depicted in Fig. 3. In endothermic mode, the current density computed with the stack environment is found to be lower than the one under isothermal condition. Conversely, above the thermoneutral voltage (i.e. exothermic operation), cell performances are enhanced. For example, at 1.4 V, the cell current density rises from ≈ -1.7 A cm⁻² in the isothermal condition to -2.4 A cm⁻² in the stack environment. The differences between both curves are related to thermally activated phenomena [68]. Indeed, the ionic conductivity of the electrolyte is strongly dependent on the temperature (+51% from 800 to 850 °C for 8YSZ [68]), in such way that any temperature increase lowers the ohmic losses and thus increases the cell performances. However, the CSC configuration investigated here displays a thin electrolyte layer and its contribution to the overall overpotential is limited. Therefore, the influence of temperature on performances is mainly explained by higher exchange current densities when the temperature is increased. Indeed, activation energies are relatively high

(Table 1) so that any temperature increase results in enhanced i_0 and lowered corresponding activation overpotential η_{act} (Equation (9)).

Finally, it is worth noting that the temperature increase does not significantly affect the cell limiting current density as shown in Fig. 3. Indeed, the limiting current is assigned to the concentration overpotentials. It is thus related to the steam starvation at the active sites caused (i) by the mass transfer limitation by diffusion across the electrode and (ii) by the thermodynamic losses due to the steam conversion rate. As already mentioned, the temperature dependence of the former diffusional process is rather weak while the latter is also very slightly dependent on the temperature. It is worth noting that steep, almost vertical limiting currents were experimentally evidenced [24] at conversion rates nearly identical to those presented in Fig. 3.

Similar general observations are made concerning the influence of temperature on co-electrolysis performances. However, the cell temperature at OCV is only about 797.5 °C (i.e. 2.5 °C less than the temperature of the gas inlets and the insulating enclosure). Indeed, the inlet cathodic composition investigated is close but does not correspond to the thermodynamic equilibrium of the WGS reaction at $T = 800$ °C. As a consequence, thermal sinks due to the chemical reaction have a small but noticeable impact on both the cell temperature and the gas composition along the cell at OCV. A more significant influence can be anticipated by changing the inlet composition. Furthermore, because of CO₂ electrolysis and WGS reaction, the thermoneutral voltage is shifted compared to H₂O electrolysis. In the present simulated conditions, the thermoneutral voltage is found to be about 1.32 V. This condition is fulfilled when the sum of the chemical and electrochemical heat sources is nil. In that case, the simulated cell temperature is then found to be equal to the furnace temperature. As expected [41], this value is comprised between the lower bound corresponding to the pure steam electrolysis (1.29 V) and the upper bound given by the pure CO₂ electrolysis (1.46 V) at 800 °C.

H₂O electrolysis operating maps

H₂O electrolysis operating maps for steam conversion rates, current densities, H₂ production and temperatures taken at the middle of the cell length are reported in Fig. 4A–D, respectively. These output parameters of the model are plotted as function of the cell voltage and the cathodic flow rate.

The simulated operating conditions (Table 2) lead to a wide range of steam conversion rates, from 0 to about 97% (Fig. 4A). At a given flow rate, increasing the cell voltage, and thus the current density, enhances the steam faradaic conversion rate (Fig. 4A). In addition, higher cathodic fluxes yield lower conversion rates, regardless of the cell voltage. For example, the conversion rate at 1.3 V decreases from 40% to 20% when the gas flux is increased by a factor 2.2, from 28.5 to 61.3 Nml min⁻¹ cm⁻².

Again assuming no gas leakage and an ideal current efficiency, the H₂ production is directly proportional to the current density through the Faraday law. Thus, Fig. 4B and C only differ by a scale factor. As it can be noticed under

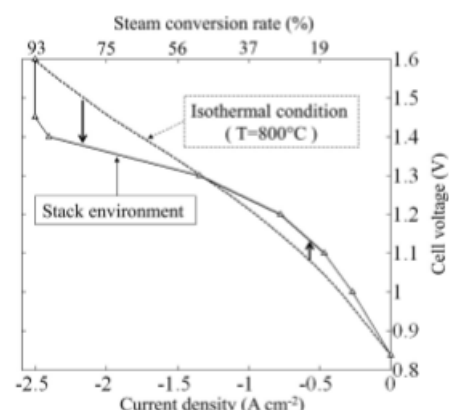


Fig. 3 – Influence of the temperature on performances (H₂O electrolysis, conditions A1). Comparison between the polarization curve obtained for the stack and the one simulated with isothermal operating condition.

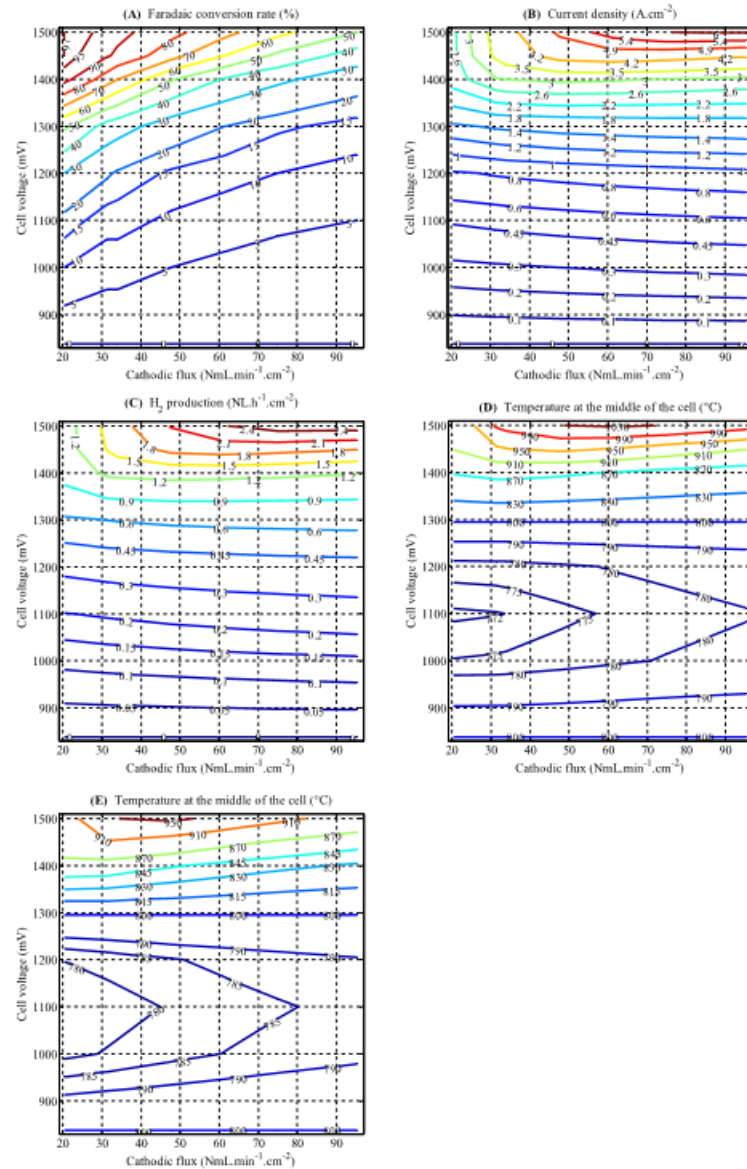


Fig. 4 – H₂O electrolysis operating maps: (A) conversion rate, (B) current density, (C) H₂ production, (D) temperature calculated at the middle of the cell length (input data given in Tables 1 and 2). Cartography (E) corresponds to the temperature at the middle of the cell when the anodic air flow rate is multiplied by three (the other input parameters remaining unchanged).

low and intermediate overpotentials, current densities and steam conversion are barely influenced by the cathodic inlet flowrate. Still, due to lowered concentration overpotentials, slightly higher current densities are obtained with higher flowrates. Conversely, at high overpotentials, it is found that the current density is strongly increased by increasing the flow rate. Indeed, under such condition of polarization, the concentration overpotentials are large enough to become prevalent among the other cell losses. In that condition, the highest steam conversion rate obtained at the limiting current is reached for the lowest investigated cathodic flowrate.

The three thermal regimes are visible on Fig. 4-D, for cell voltages above and below 1.29 V. However, it can be noticed that increasing the gas flowrate has limited impact on the calculated temperatures. Indeed, it was shown that, in the chosen conditions, the radiative exchanges with the insulation dominate heat transfer over convection [48]. Nevertheless, under endothermic conditions, one can note that increasing flowrates yield slightly higher temperatures. Indeed, for cell voltages below 1.29 V, current densities remain relatively independent of the flowrate (Fig. 4-B) meaning that the heat absorption by the reactions is nearly constant regardless of the flowrates. Therefore, the slight temperature elevation with increasing flowrates is explained by convective heat transfer from the inlet gas to the SRU. When the SRU operates in the exothermic mode, the same phenomenon also explains the slight decrease of temperatures with higher flowrates. However, this last statement does not apply when the cell voltage $U_{\text{cell}} > 1.4$ V and the flowrate $F < 50$ Nml min⁻¹ cm⁻². Indeed, in this narrow region of operating conditions, current densities increase quickly with higher flowrates, leading to more heat released in the cell and overcompensating the increase of the convective exchanges.

Within the scope of this study, the cooling of the cell in endothermic operation is found reasonable. Indeed, the coldest temperature obtained under a flowrate of 20 Nml min⁻¹ cm⁻² is 770 °C. In these conditions, thermal phenomena have a limited impact on the electrolyzer global response. However, in exothermic operating mode, temperatures exceed 850 °C for cell voltages higher than ≈ 1.35 V. It is worth noting that such extreme temperature elevation should be avoided to preserve the stack integrity. Indeed, these high temperatures will most certainly be detrimental to the material stability by accelerating all thermally activated processes of degradation such as Ni agglomeration, material reactivity between cell components, etc. [68]. Moreover, the level of cell temperature strongly depends on the system design and the assigned boundary conditions. In the present work, it is assumed that the stack can exchange heat by radiation with a thermally regulated insulating enclosure. That condition leads to cushion the cell warming in the exothermic mode of operation (since a part of the dissipated heat can be absorbed by the insulation). For a system design without thermal regulation, the generated heat can be only removed by the gas flows so that the temperature rise will be much steeper. Therefore, the temperature elevation presented in Fig. 2 can be regarded as a lower bounds for different system designs.

In order to mitigate the stack temperature elevation without affecting too much the performances, one solution could consist of increasing the air sweeping at the anode side.

To investigate this possibility, simulations have been carried out after increasing the flow rate at the anode side by a factor of three (all the other input model parameters remaining unchanged). As shown in Fig. 4-E, the improved convective heat exchange at the anode side allows to reduce significantly the temperature in the exothermic mode of operation. Therefore, this approach appears to be an interesting method to extend as much as possible the stack operation beyond the thermo-neutral voltage.

Whatever the mitigating solution, the stack must be operated in safe operating conditions in order to preserve a reasonable temperature, below 850 °C [68]. Regarding the operating cartographies presented in Fig. 4-D or E, this leads to restrict the cell polarization below around 1.35 V. Furthermore, for an electrolyzer to be economically viable, steam conversion rates should be kept above 50% [69]. These two main constraints determine the optimum operating conditions for H₂O electrolysis: $1.29 < U_{\text{cell}} < 1.35$ V, and $20 < F_{\text{cathode}} < 40$ Nml min⁻¹ cm⁻².

Within such range of optimum operating conditions, a 25-cell stack with an active area of 100 cm² per cell operated at 1.3 V and 20 Nml min⁻¹ cm⁻² would yield a current density of -1.4 A cm⁻², a 50% conversion rate, and a H₂ production rate of 1.5 Nm³ h⁻¹. In these conditions, the calculated electrolyzer temperature would be about 800 °C, simplifying the stack thermal management. The electrical efficiency, defined as the ratio between the energy contained in the produced hydrogen over the consumed electrical power, reaches 96% (note that this definition of the electrical efficiency is only relevant for a free and available source of heat). Comparatively, electrical efficiencies of alkaline and PEM electrolyzers are about 62 and 68%, respectively [68]. Nevertheless, it can be pointed out that the SOC durability submitted to a rather high current density of -1.4 A cm⁻² remains to be checked. If the degradation rate turns out to be too high for such operating conditions, one solution could consist to lower the inlet flow rate below 20 Nml min⁻¹ cm⁻². At 1.3 V, the conversion rate will be then higher than 50% and the electrical efficiency will strictly remain unchanged to 96% (it does not depend on the current). However, in this case, the hydrogen production rate per stack will be lowered.

Co-electrolysis operating maps

Co-electrolysis operating maps for current densities, conversion rates, syngas productions and temperatures are given in Fig. 5A–D, respectively. It can be noticed that the set of parameters investigated (Table 2) leads here to a 0–96% range of conversion rates. Similarly to H₂O electrolysis mode, at a given cell voltage, increasing the cathodic flux yields slightly higher current densities (Fig. 5-A). Once again, this is due to lower concentration overpotentials as lower conversion rates are obtained (Fig. 5-B). Despite the slight increase, current densities are found to be globally stable as functions of inlet flowrates, especially when $F_{\text{cathode}} > 20$ Nml min⁻¹ cm⁻². Consequently, global heat source terms and resulting cell temperatures (Fig. 5-D) only marginally depend on inlet flowrates. Indeed, the enthalpies of dissociation of H₂O and CO₂ are comparable and, in absolute, greatly superior to the enthalpy of the WGS reaction. The co-electrolysis current

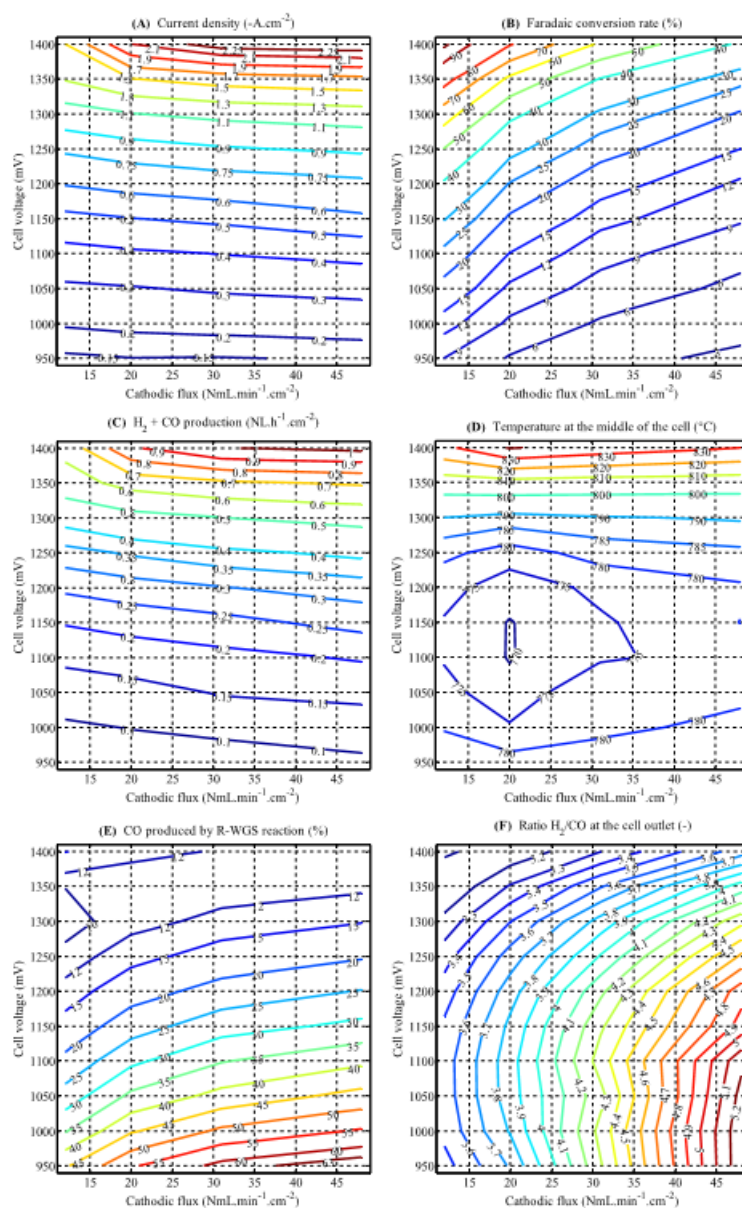


Fig. 5 – Co-electrolysis operating maps: (A) current density, (B) conversion rate, (C) syngas production, (D) temperature taken at the middle of the cell length, (E) CO produced by the reverse WGS reaction, (F) H₂/CO at the cell outlet.

density, with its corresponding cell voltage, thus governs heat generation, and as aforementioned, is stable over the parametric range of this study. In addition, syngas H_2+CO production profiles also follow those of the current densities (Fig. 5-C) and are independent of the rate of WGS reaction. Indeed, this chemical reaction is equi-molar and consumes one molecule of CO to produce one of H_2 (and vice-versa). In that condition, the WGS reaction cannot change the total flux of the produced syngas even if it can affect its composition.

Fig. 5-E presents the global influence of the WGS reaction on the co-electrolysis process, through the relative proportion of carbon monoxide produced via chemical reaction (5) in regards to the global (i.e. chemical and electrochemical) production. Therefore, values can be negative in the case of a chemical reaction globally consuming CO . As showed in Fig. 5-E, only positive values are calculated, supporting a WGS reaction globally in the “reverse” direction. It can be noticed that this does not necessarily mean that the WGS reaction operates in the reverse direction everywhere within the thick cathode substrate [21,44]. As previously evidenced for low inlet flowrates [44], the amount of CO produced by the reverse WGS reaction increases with the cathodic flowrate (i.e. lower conversion rate), whereas its contribution is a decreasing function of the cell voltage. For instance, only a fourth of the produced CO is found to originate from the reverse WGS reaction at 1.2 V, even by increasing the cathodic flow rate up to $48 \text{ NmL min}^{-1} \text{ cm}^{-2}$. The hereby found prevalence of CO_2 electrolysis on the WGS reaction over CO production is discussed in greater detail in a previous work [24]. However, because the contribution of the reverse WGS reaction is never negligible, the H_2/CO ratio at the cell outlet depends on operating conditions (i.e. inlet flowrate and composition, temperature, cell voltage, etc.), as seen on Fig. 5-F.

These operating maps can be used to determine optimal operating conditions regarding a complete Power-to-Fuel process. In light of the preceding results, the minimum acceptable conversion rate is likely to be the most relevant parameter for co-electrolysis operation. Additionally, very

high current densities (i.e. $>|-2| \text{ A cm}^{-2}$) may be avoided when using a nickel based cermet since it was shown that it could lead to carbon deposition [70,71]. Thus, within the investigated range, one could argue that $20 \text{ NmL min}^{-1} \text{ cm}^{-2}$ at 1.35 V could be a middle ground for practical operations, yielding -1.5 A cm^{-2} and 60% conversion rate. This co-electrolyzer would then operate at about 810°C , in a slightly exothermic mode. This would therefore only marginally lower the cell electrical efficiency, while the extra heat could allow preheating inlet gases. Using these values, the global output of a 25-cell stack co-electrolyzer would correspond to a 5 kW electrical power, and would produce $1.63 \text{ Nm}^3 \text{ h}^{-1}$ of syngas with a H_2/CO outlet ratio of 3.3.

Comparison of H_2O electrolysis and Co-Electrolysis

Comparing H_2O and H_2O+CO_2 electrolysis operating maps highlights several striking differences. First, in the same condition of inlet flow rate and cell voltage, the current density reached in co-electrolysis is lower than the one obtained in steam electrolysis. In agreement with experimental reports [13,24], H_2O electrolysis displays higher performances and thus higher conversion rates than co-electrolysis at given flowrate and cell voltage. This difference becomes especially pronounced when approaching the highest overpotentials investigated. This stems from more severe mass transport limitations due to the multicomponent (H_2 , H_2O , CO and CO_2) diffusion in the thick porous cathode. Conversely, under pure steam electrolysis, the diffusion of H_2O and H_2 is less limiting so that higher current densities are reached, leading to higher SRU temperature elevations, and in turn, to faster electrochemical kinetics. Such difference could constitute an overall limitation of the co-electrolysis process, especially when the cathode microstructure has not been carefully optimized.

However, the globally lower current densities obtained in co-electrolysis mode could have positive repercussions on the SRU/stack thermal management. Indeed, the maximum temperature elevation obtained in co-electrolysis is limited to

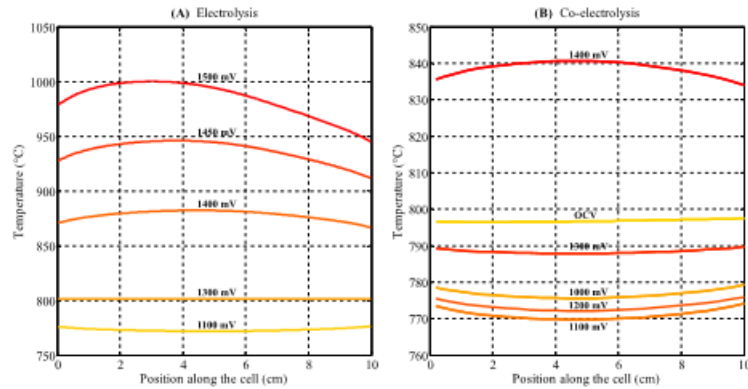


Fig. 6 – Longitudinal evolutions of cell temperature as a function of the cell voltage when the cell is fed with (A) $20 \text{ NmL min}^{-1} \text{ cm}^{-2}$ of 90/10 vol.% H_2O/H_2 and (B) 65/25/10 vol.% $H_2O/CO_2/H_2$.

+40 °C compared to 800 °C (Fig. 5-D), which is significantly less than for H₂O electrolysis (Fig. 4-D). In light of the previously discussed influence of current densities on temperatures, both electrolysis modes can be compared in greater details when $F_{\text{cathode}} = 20 \text{ Nml min}^{-1} \text{ cm}^{-2}$. Indeed, under such feeding conditions, current densities in both H₂O electrolysis and co-electrolysis modes are roughly identical with regards to the cell voltage. Fig. 6 shows the computed longitudinal temperature profiles obtained in conditions A1 and B2 (Table 2). As can be seen, temperature elevations and gradients are significantly reduced in co-electrolysis mode compared to H₂O electrolysis operation. For example, at 1.4 V, middle cell temperatures are about 840 and 860 °C, while differences between hottest and coldest local temperatures are about 5 and 20 °C in co-electrolysis and H₂O electrolysis modes, respectively.

Such differences in cell temperatures and thermal profiles could be explained by several factors. First, as previously discussed, the thermoneutral voltage in co-electrolysis is dependent on inlet gas composition and is shifted toward higher voltages compared to steam electrolysis. Considering inlet composition 65/25/10 vol.% H₂O/CO₂/H₂, it is evaluated here to about 1.32 V. This means that any given operating cell voltage in the exothermic mode will be closer to the thermoneutral voltage in co-electrolysis mode than in H₂O electrolysis. Such phenomenon includes the slightly endothermic reverse WGS reaction, favored in the simulated conditions (Fig. 5-E). In addition, the volumetric heat capacity of the cathode gas mixture is increased in co-electrolysis operation. Indeed, both CO and CO₂ display greater C_p (33.7 and 55.4 J mol⁻¹ K⁻¹ respectively [72]) than H₂ and H₂O (30.3 and 42.4 J mol⁻¹ K⁻¹ [72]), respectively. Thus, cathode gas flows are able to evacuate more heat in co-electrolysis than in H₂O electrolysis, positively affecting temperatures and thermal gradients.

Besides the obvious advantage of co-electrolysis for a direct production of syngas, these results suggest an easier thermal management compared to steam electrolysis, especially crucial in stack environment. Co-electrolysis could thus exhibit a wider range of acceptable operating conditions compared to H₂O electrolysis, since high thermal gradients have been shown to cause mechanical stress, potentially leading to cell failure [51].

Conclusions

Experimentally validated H₂O electrolysis and H₂O–CO₂ co-electrolysis models have been used to assess the technological potential of high temperature electrolysis through the establishment of operating maps. Cartographies have been computed for inlet cathode compositions 90/10 vol.% H₂O/H₂ and 65/25/10 vol.% H₂O/CO₂/H₂. The multiple inlet flowrates simulated ensured covering a wide range of conversion rates, up to about 96%. Based on the sets of simulations, a domain of optimized operating conditions has been identified for both processes. They allow achieving relatively high conversion rates while keeping a reasonable stack temperature.

The simulated results have been analyzed with the objective of comparing the relative advantages and drawbacks of

co-electrolysis and electrolysis. In accordance with experimental observations [13,24], co-electrolysis performances are found to be lower than those of H₂O electrolysis in similar conditions. Accordingly, the temperature elevation above the thermos-neutral voltage in electrolysis is found to be much more pronounced compared to co-electrolysis. In addition, it was found that longitudinal thermal gradients are steeper in H₂O electrolysis, resulting in potentially harsher mechanical stresses and material degradation rates. In the exothermic part of the computed co-electrolysis polarization curves, the benefits from higher temperature, which could have yielded higher current densities, are hindered by strong mass transport limitations. Indeed, a maximum current density was simulated, resulting in large drops of conversion rates when the cathodic flowrate was increased. Therefore, studies devoted to microstructure optimization of the cell support to enhance CO/CO₂ gas transport should constitute a promising way to improve cell efficiency in co-electrolysis operation.

In addition, over the complete set of simulations, CO₂ electroreduction was found to account for most of the CO production, as CO generated by the reversed WGS reaction was only in the 10–15% range at 1.3 V. Furthermore, the outlet ratio H₂/CO was shown to depend on current density, inlet cathodic flowrate and temperature. These parameters could all be adjustable variables to obtain a specific outlet gas composition, in view of a coupling with a specific post-electrolyzer process (e.g. methanation reaction).

Acknowledgments

The contribution of F. Loisy to this work is gratefully acknowledged. The research leading to these results has received funding from KIC InnoEnergy (Minerve project, Grant Agreement 76_2012_IP35_MINERVE) and from the European Union's 7th Framework Program (FP7/2007-2013) Fuel Cells and Hydrogen Joint Undertaking (FGH-JU-2013-1) under grant agreement n°621173 (SOPHIA project).

REFERENCES

- [1] O'Brien JE. Considerations for thermal water splitting processes and high temperature electrolysis. In: Proc 2008 Int Mech Eng Congr Expo; 2008.
- [2] Kim-Lohsoontorn P, Laosiripojana N, Bae J. Performance of solid oxide electrolysis cell having bi-layered electrolyte during steam electrolysis and carbon dioxide electrolysis. Curr Appl Phys 2011;11:S223–8. <http://dx.doi.org/10.1016/j.cap.2010.11.114>.
- [3] Tao G, Sridhar KR, Chan CL. Study of carbon dioxide electrolysis at electrode/electrolyte interface: Part I. Pt/YSZ interface. Solid State Ion 2004;175:615–9. <http://dx.doi.org/10.1016/j.ssi.2004.01.077>.
- [4] Zhan Z, Zhao L. Electrochemical reduction of CO₂ in solid oxide electrolysis cells. J Power Sources 2010;195:7250–4. <http://dx.doi.org/10.1016/j.jpowsour.2010.05.037>.
- [5] Ebbesen SD, Mogensen M. Electrolysis of carbon dioxide in solid oxide electrolysis cells. J Power Sources 2009;193:349–58. <http://dx.doi.org/10.1016/j.jpowsour.2009.02.093>.

- [6] Dry ME. The Fischer–Tropsch process: 1950–2000. *Fischer–Tropsch Synth* 2002;71:227–41. [http://dx.doi.org/10.1016/S0920-5861\(01\)00453-9](http://dx.doi.org/10.1016/S0920-5861(01)00453-9).
- [7] Becker WL, Braun RJ, Penev M, Melaina M. Production of Fischer–Tropsch liquid fuels from high temperature solid oxide co-electrolysis units. *Energy* 2012;47:99–115. <http://dx.doi.org/10.1016/j.energy.2012.08.047>.
- [8] Graves C, Ebbesen SD, Mogensen M, Lackner KS. Sustainable hydrocarbon fuels by recycling CO₂ and H₂O with renewable or nuclear energy. *Renew Sustain Energy Rev* 2011;15:1–23. <http://dx.doi.org/10.1016/j.rser.2010.07.014>.
- [9] Fu Q, Mabilat C, Zahid M, Brisse A, Gautier L. Syngas production via high-temperature steam/CO₂ co-electrolysis: an economic assessment. *Energy Environ Sci* 2010;3:1382. <http://dx.doi.org/10.1039/c0ee00092b>.
- [10] Iskov H, Rasmussen NB. Global screening of projects and technologies for Power-to-Gas and Bio-SNG. 2013. http://www.dgc.dk/sites/default/files/filer/publikationer/R1307_screening_projects.pdf.
- [11] Xu J, Froment GF. Methane steam reforming, methanation and water-gas shift: I. Intrinsic kinetics. *AIChE J* 1989;35:88–96. <http://dx.doi.org/10.1002/aic.690350109>.
- [12] Kim-Lohsontorn P, Bae J. Electrochemical performance of solid oxide electrolysis cell electrodes under high-temperature coelectrolysis of steam and carbon dioxide. *J Power Sources* 2011;196:7161–8. <http://dx.doi.org/10.1016/j.jpowsour.2010.09.018>.
- [13] Graves C, Ebbesen SD, Mogensen M. Co-electrolysis of CO₂ and H₂O in solid oxide cells: performance and durability. *Solid State Ion* 2011;192:398–403. <http://dx.doi.org/10.1016/j.ssi.2010.06.014>.
- [14] Nguyen VN, Fang Q, Packbier U, Blum L. Long-term tests of a Jülich planar short stack with reversible solid oxide cells in both fuel cell and electrolysis modes. *Int J Hydrog Energy* 2013;38:4281–90. <http://dx.doi.org/10.1016/j.ijhydene.2013.01.192>.
- [15] Ebbesen SD, Høgh J, Nielsen KA, Nielsen JU, Mogensen M. Durable SOC stacks for production of hydrogen and synthesis gas by high temperature electrolysis. *Int J Hydrog Energy* 2011;36:7363–73. <http://dx.doi.org/10.1016/j.ijhydene.2011.03.130>.
- [16] Chen M, Liu Y-L, Bentzen JJ, Zhang W, Sun X, Hauch A, et al. Microstructural degradation of Ni/YSZ electrodes in solid oxide electrolysis cells under high current. *J Electrochem Soc* 2013;160:F883–91. <http://dx.doi.org/10.1149/2.098308jes>.
- [17] Lay-Grindler E, Laurencin J, Villanova J, Cloetens P, Bleuet P, Mansuy A, et al. Degradation study by 3D reconstruction of a nickel–yttria stabilized zirconia cathode after high temperature steam electrolysis operation. *J Power Sources* 2014;269:927–36. <http://dx.doi.org/10.1016/j.jpowsour.2014.07.066>.
- [18] Ebbesen SD, Mogensen M. Exceptional durability of solid oxide cells. *Electrochem Solid-State Lett* 2010;13:B106. <http://dx.doi.org/10.1149/1.3455882>.
- [19] Graves C, Ebbesen SD, Jensen SH, Simonsen SB, Mogensen MB. Eliminating degradation in solid oxide electrochemical cells by reversible operation. *Nat Mater* 2014;14:239–44. <http://dx.doi.org/10.1038/nmat4165>.
- [20] Hjalmarsson P, Sun X, Liu Y-L, Chen M. Influence of the oxygen electrode and inter-diffusion barrier on the degradation of solid oxide electrolysis cells. *J Power Sources* 2013;223:349–57. <http://dx.doi.org/10.1016/j.jpowsour.2012.08.063>.
- [21] Aicart J. Modeling and experimental validation of steam and carbon dioxide Co-electrolysis at high temperature. PhD Thesis Grenoble-Alpes. 2014.
- [22] Di Iorio S, Petitjean M, Petit J, Chatroux A, Gousseau G, Aicart J, et al. SOE stack activities at CEA. In: *Proceeding 11th Eur SOFC Forum* Lucerne; 2014.
- [23] Al Daroukh M, Tietz F, Sebold D, Buchkremer HP. Post-test analysis of electrode-supported solid oxide electrolyser cells. *Ionics* 2015;21:1039–43. <http://dx.doi.org/10.1007/s11581-014-1273-2>.
- [24] Aicart J, Petitjean M, Laurencin J, Talloire L, Dessemond L. Accurate predictions of H₂O and CO₂ co-electrolysis outlet compositions in operation. *Int J Hydrog Energy* 2015;40:3134–48. <http://dx.doi.org/10.1016/j.ijhydene.2015.01.031>.
- [25] Reyrier M, Di Iorio S, Chatroux A, Petitjean M, Cren J, De Saint Jean M, et al. Stack performances in high temperature steam electrolysis and co-electrolysis. *Int J Hydrog Energy* 2015;40:11370–7. <http://dx.doi.org/10.1016/j.ijhydene.2015.04.085>.
- [26] Wood A, He H, Joia T, Krivy M, Steedman D. Communication—Electrolysis at high efficiency with remarkable hydrogen production rates. *J Electrochem Soc* 2016;163:F327–9. <http://dx.doi.org/10.1149/2.0341605jes>.
- [27] Stoots C, O'Brien J, Hartvigsen J. Results of recent high temperature coelectrolysis studies at the Idaho National Laboratory. *Int J Hydrog Energy* 2009;34:4208–15. <http://dx.doi.org/10.1016/j.ijhydene.2008.08.029>.
- [28] Zheng Y, Chen T, Li Q, Wu W, Miao H, Xu C, et al. Achieving 360 NL h^{−1} hydrogen production rate through 30-Cell solid oxide electrolysis stack with LSCF–GDC composite oxygen electrode. *Fuel Cells* 2014;14:1066–70. <http://dx.doi.org/10.1002/fuce.201400051>.
- [29] Zheng Y, Li Q, Guan W, Xu C, Wu W, Wang WG. Investigation of 30-cell solid oxide electrolyzer stack modules for hydrogen production. *Ceram Int* 2014;40:5801–9. <http://dx.doi.org/10.1016/j.ceramint.2013.11.020>.
- [30] Zhang X, O'Brien JE, Tao G, Zhou C, Housley GK. Experimental design, operation, and results of a 4 kW high temperature steam electrolysis experiment. *J Power Sources* 2015;297:90–7. <http://dx.doi.org/10.1016/j.jpowsour.2015.07.098>.
- [31] Ni M, Leung MKH, Leung DYC. Mathematical modeling of the coupled transport and electrochemical reactions in solid oxide steam electrolyzer for hydrogen production. *Electrochim Acta* 2007;52:6707–18. <http://dx.doi.org/10.1016/j.electacta.2007.04.084>.
- [32] Udagawa J, Aguiar P, Brandon NP. Hydrogen production through steam electrolysis: model-based steady state performance of a cathode-supported intermediate temperature solid oxide electrolysis cell. *J Power Sources* 2007;166:127–36. <http://dx.doi.org/10.1016/j.jpowsour.2006.12.081>.
- [33] Udagawa J, Aguiar P, Brandon NP. Hydrogen production through steam electrolysis: model-based dynamic behaviour of a cathode-supported intermediate temperature solid oxide electrolysis cell. *J Power Sources* 2008;180:46–55. <http://dx.doi.org/10.1016/j.jpowsour.2008.02.026>.
- [34] Ni M. Computational fluid dynamics modeling of a solid oxide electrolyzer cell for hydrogen production. *Int J Hydrog Energy* 2009;34:7795–806. <http://dx.doi.org/10.1016/j.ijhydene.2009.07.080>.
- [35] Boëdec T, Reyrier M, Lhachemi D, Tschumperlé D, Louat P, Di Iorio S, et al. A new stack to validate technical solutions and numerical simulations. *Fuel Cells* 2012;12:239–47. <http://dx.doi.org/10.1002/fuce.201100078>.
- [36] Grondin D, Deseure J, Ozil P, Chabriet J-P, Grondin-Perez B, Brisse A. Computing approach of cathodic process within solid oxide electrolysis cell: experiments and continuum model validation. *J Power Sources* 2011;196:9561–7. <http://dx.doi.org/10.1016/j.jpowsour.2011.07.033>.

- [37] Lay-Grindler E, Laurencin J, Delette G, Aicart J, Petitjean M, Dessemont L. Micro modelling of solid oxide electrolysis cell: from performance to durability. *Int J Hydrog Energy* 2013;38:6917–29. <http://dx.doi.org/10.1016/j.ijhydene.2013.03.162>.
- [38] Stoots CM, O'Brien JE, Condie KG, Hartvigsen JJ. High-temperature electrolysis for large-scale hydrogen production from nuclear energy – experimental investigations. *Int J Hydrog Energy* 2010;35:4861–70. <http://dx.doi.org/10.1016/j.ijhydene.2009.10.045>.
- [39] Ni M. An electrochemical model for syngas production by co-electrolysis of H_2O and CO_2 . *J Power Sources* 2012;202:209–16. <http://dx.doi.org/10.1016/j.jpowsour.2011.11.080>.
- [40] O'Brien JE, McKellar MG, Stoots CM, Herring JS, Hawkes GL. Parametric study of large-scale production of syngas via high-temperature co-electrolysis. *Int J Hydrog Energy* 2009;34:4216–26. <http://dx.doi.org/10.1016/j.ijhydene.2008.12.021>.
- [41] Sun X, Chen M, Jensen SH, Ebbesen SD, Graves C, Mogensen M. Thermodynamic analysis of synthetic hydrocarbon fuel production in pressurized solid oxide electrolysis cells. *Int J Hydrog Energy* 2012;37:17101–10. <http://dx.doi.org/10.1016/j.ijhydene.2012.08.125>.
- [42] Ni M. 2D thermal modeling of a solid oxide electrolyzer cell (SOEC) for syngas production by H_2O/CO_2 co-electrolysis. *Int J Hydrog Energy* 2012;37:6389–99. <http://dx.doi.org/10.1016/j.ijhydene.2012.01.072>.
- [43] Aicart J, Laurencin J, Petitjean M, Dessemont L. Experimental validation of Co-electrolysis modeling. In: *Proc 2013 EFCF Congr*; 2013.
- [44] Aicart J, Laurencin J, Petitjean M, Dessemont L. Experimental validation of two-dimensional H_2O and CO_2 Co-electrolysis modeling. *Fuel Cells* 2014;14:430–47. <http://dx.doi.org/10.1002/fuce.201300214>.
- [45] Menon V, Fu Q, Janardhanan VM, Deutschmann O. A model-based understanding of solid-oxide electrolysis cells (SOECs) for syngas production by H_2O/CO_2 co-electrolysis. *J Power Sources* 2015;274:768–81. <http://dx.doi.org/10.1016/j.jpowsour.2014.09.158>.
- [46] Kazempoor P, Braun RJ. Hydrogen and synthetic fuel production using high temperature solid oxide electrolysis cells (SOECs). *Int J Hydrog Energy* 2015;40:3599–612. <http://dx.doi.org/10.1016/j.ijhydene.2014.12.126>.
- [47] Diethelm S, Herle JV, Montinaro D, Bucheli O. Electrolysis and Co-electrolysis performance of SOE short stacks. *Fuel Cells* 2013;13:631–7. <http://dx.doi.org/10.1002/fuce.201200178>.
- [48] Laurencin J, Kane D, Delette G, Deseure J, Lefebvre-Joud F. Modelling of solid oxide steam electrolyser: impact of the operating conditions on hydrogen production. *J Power Sources* 2011;196:2080–93. <http://dx.doi.org/10.1016/j.jpowsour.2010.09.054>.
- [49] Weber A, Ivers-Tiffée E. Materials and concepts for solid oxide fuel cells (SOFCs) in stationary and mobile applications. *Eighth Int Electrochem Tag* 2004;127:273–83. <http://dx.doi.org/10.1016/j.jpowsour.2003.09.024>.
- [50] Park K, Yu S, Bae J, Kim H, Ko Y. Fast performance degradation of SOFC caused by cathode delamination in long-term testing. *Int J Hydrog Energy* 2010;35:8670–7. <http://dx.doi.org/10.1016/j.ijhydene.2010.05.005>.
- [51] Usseglio-Viretta F. Optimisation des performances et de la robustesse d'un électrolyseur à hautes températures. PhD Thesis Grenoble-Alpes. 2015.
- [52] Klotz D, Leonide A, Weber A, Ivers-Tiffée E. Electrochemical model for SOFC and SOEC mode predicting performance and efficiency. *Int J Hydrog Energy* 2014;39:20844–9. <http://dx.doi.org/10.1016/j.ijhydene.2014.08.139>.
- [53] Cast3M n.d. <http://www-cast3m cea.fr/>.
- [54] Li W, Wang H, Shi Y, Cai N. Performance and methane production characteristics of H_2O-CO_2 co-electrolysis in solid oxide electrolysis cells. *Int J Hydrog Energy* 2013;38:11104–9. <http://dx.doi.org/10.1016/j.ijhydene.2013.01.008>.
- [55] Lee WY, Hanna J, Ghoniem AF. On the predictions of carbon deposition on the nickel anode of a SOFC and its impact on open-circuit conditions. *J Electrochem Soc* 2012;160:F94–105. <http://dx.doi.org/10.1149/2.051302jes>.
- [56] Kim J-W. Polarization effects in intermediate temperature, anode-supported solid oxide fuel cells. *J Electrochem Soc* 1999;146:69. <http://dx.doi.org/10.1149/1.1391566>.
- [57] Adler SB. Mechanism and kinetics of oxygen reduction on porous $La_{1-x}Sr_xCoO_{3-\delta}$ electrodes. *Solid State Ion* 1998;111:125–34. [http://dx.doi.org/10.1016/S0167-2738\(98\)00179-9](http://dx.doi.org/10.1016/S0167-2738(98)00179-9).
- [58] Primdahl S, Mogensen M. Oxidation of hydrogen on Ni/yttria-stabilized zirconia cermet anodes. *J Electrochem Soc* 1997;144:3409–19.
- [59] Usseglio-Viretta F, Laurencin J, Delette G, Villanova J, Cloetens P, Leguillon D. Quantitative microstructure characterization of a Ni-YSZ bi-layer coupled with simulated electrode polarisation. *J Power Sources* 2014;256:394–403. <http://dx.doi.org/10.1016/j.jpowsour.2014.01.094>.
- [60] Menon V, Janardhanan VM, Deutschmann O. Modeling of solid-oxide electrolyser cells: from H_2 , CO electrolysis to Co-electrolysis. *ECS Trans* 2013;57:3207–16. <http://dx.doi.org/10.1149/05701.3207ecst>.
- [61] Suwanwarangkul R, Croiset E, Fowler MW, Douglas PL, Entchev E, Douglas MA. Performance comparison of Fick's, dusty-gas and Stefan–Maxwell models to predict the concentration overpotential of a SOFC anode. *J Power Sources* 2003;122:9–18. [http://dx.doi.org/10.1016/S0378-7753\(02\)00724-3](http://dx.doi.org/10.1016/S0378-7753(02)00724-3).
- [62] Laurencin J, Lefebvre-Joud F, Delette G. Impact of cell design and operating conditions on the performances of SOFC fuelled with methane. *J Power Sources* 2008;177:355–68. <http://dx.doi.org/10.1016/j.jpowsour.2007.11.099>.
- [63] Ackmann T, de Haart LGJ, Lehnert W, Stolten D. Modeling of mass and heat transport in planar substrate type SOFCs. *J Electrochem Soc* 2003;150:A783. <http://dx.doi.org/10.1149/1.1574029>.
- [64] Veldsink JW, van Damme RMJ, Versteeg GF, van Swaaij WPM. The use of the dusty-gas model for the description of mass transport with chemical reaction in porous media. *Chem Eng J Biochem Eng J* 1995;57:115–25. [http://dx.doi.org/10.1016/0923-0467\(94\)02929-6](http://dx.doi.org/10.1016/0923-0467(94)02929-6).
- [65] Fuller EN, Schettler PD, Giddings JC. New method for prediction of binary gas-phase diffusion coefficients. *Ind Eng Chem* 1966;58:18–27. <http://dx.doi.org/10.1021/ie50677a007>.
- [66] Mougín J, Chatroux A, Couturier K, Petitjean M, Reyrier M, Gousseau G, et al. High temperature steam electrolysis stack with enhanced performance and durability. *Energy Procedia* 2012;29:445–54. <http://dx.doi.org/10.1016/j.egypro.2012.09.052>.
- [67] Mougín J, Mansuy A, Chatroux A, Gousseau G, Petitjean M, Reyrier M, et al. Enhanced performance and durability of a high temperature steam electrolysis stack. *Fuel Cells* 2013;13:623–30. <http://dx.doi.org/10.1002/fuce.201200199>.
- [68] Laurencin J, Mougín J. *Chp 6-Hydrogen production: by electrolysis*. John Wiley & Sons; 2015.
- [69] De Saint Jean M. Étude énergétique et évaluation économique d'une boucle de stockage - déstockage d'énergie électrique d'origine renouvelable sur méthane de synthèse à l'aide d'un convertisseur électrochimique réversible SOEC – SOFC. PhD Thesis. MINES ParisTech; 2014.
- [70] Tao Y, Ebbesen SD, Zhang W, Mogensen MB. Carbon nanotube growth on nanozirconia under strong cathodic polarization in steam and carbon dioxide. *ChemCatChem* 2014;6:1220–4. <http://dx.doi.org/10.1002/cctc.201300941>.
- [71] Tao Y, Ebbesen SD, Mogensen MB. Carbon deposition in solid oxide cells during Co-electrolysis of H_2O and CO_2 . *J Electrochem Soc* 2014;161:F337–43. <http://dx.doi.org/10.1149/2.079403jes>.
- [72] Todd B, Young JB. Thermodynamic and transport properties of gases for use in solid oxide fuel cell modelling. *J Power Sources* 2002;110:186–200. [http://dx.doi.org/10.1016/S0378-7753\(02\)00277-X](http://dx.doi.org/10.1016/S0378-7753(02)00277-X).

中文翻译

固体氧化物电解池高温共电解 H_2O 与 CO_2

摘要

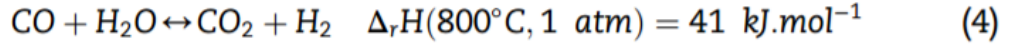
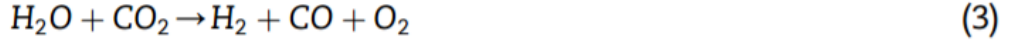
该工作旨在通过建模方法研究固体氧化物电解池中高温电解 H_2O 和电解 $\text{H}_2\text{O} + \text{CO}_2$ 之间的电化学差异。将具有典型平面堆叠的阴极支撑型电池进行研究，并讨论了局部温度对极化曲线的影响。根据电池电压和入口气体流量，对电解模式进行操作图模拟，涵盖了气体转化率的完整范围，确定了高效的最佳操作条件。总体而言，蒸汽电解中发现了较高的性能，研究发现共电解过程受到厚阴极的质量传输的限制。最后，通过调整操作参数可以灵活地调节共电解产生的合成气的组成。

引言

公众对环境压力认识的提高，目前的石油/天然气/煤能源转换系统必须转向具有低碳的可再生能源。然而，长时间内存储电力仍然是一个挑战，这种转型必须依靠合适的能量载体。由于电化学转换器和相关的氢气的高能量含量和无碳影响，在不久的将来发挥重要作用。

目前，基于固体氧化物电池（SOCs）的高温蒸汽电解（HTSE）已成为主要研究课题。这种技术能够以低电力成本生产 H_2 ，因为用于水分解所需能量的一部分由热量提供。因此，如果 SOC 被供给废热^[1]，HTSE 在 800°C 下的电化学效率显示达到非常高的值。

此外，由于高的工作温度，SOC 提供电解 CO_2 以产生 CO (2) 的能力^[2-5]，并且共同电解 H_2O 和 CO_2 以产生 $\text{H}_2 + \text{CO}$ 合成气 (3)。在最后的运行模式中，水煤气变换（WGS）反应 (4) 也发生并参与 CO 生成过程。由于最终产品（如甲烷，甲醇合成石油，汽油等）容易储存并可以从合成气中分离出来，因此在电力以燃料形式存储的情况下（即通常称为电力），共电解可能对气体或液体是非常有意义的。实际上，完整的路线，(i) 使用固体吸附剂对大气 CO_2 捕获，(ii) $\text{H}_2\text{O} + \text{CO}_2$ 共同电解和 (iii) 基于 Fischer-Tropsch 过程^[6,7] 的合成燃料生产被确定为最节能和经济上可行的电力到燃料路径^[8]。虽然燃料价格， O_2 产品价值和二氧化碳成本可能是限制因素^[9]，但是通过大量正在进行的研究计划比较，全球范围内正在对电力/气体/液体潜力进行评估^[10]。高温下 H_2O 和 $\text{H}_2\text{O} + \text{CO}_2$ 电解方法可以产生有效的能量载体，从而大量实施与电力网不相连的可再生能源。



然而，为了在经济上可行，仍然需要提高 SOC 的性能、耐久性和可靠性。在这个目标下，已经开展了各种实验研究来评估运行中的 SOC 电化学反应。已经表明，在特定的操作条件下，在蒸汽和共电解中可以获得类似的性能。另外，对于特定的操作条件，电解模式通常显示出相当的降解速率。事实上，诱导电解池衰老的潜在机制与可能电解操作模式无关，例如，显示电解池解离主要是由于温度驱动的 Ni 颗粒粗化，入口气体中存在的杂质^[18]或氧气压力积聚引起的。然而，即使 SOC 的耐久性仍然需要提高，纽扣电池和堆叠水平证明了 H_2O 和 $\text{H}_2\text{O}+\text{CO}_2$ 电解过程的高性能。这些结果近来引发了大规模扩大高温电解和共电解技术的研究。然而，为了有效地操作大的有源区域堆叠（堆积单个重复单元 SRUs，每个包含一个 SOC），仍然需要更好地了解热现象及其对性能和出口组成的影响。为此，建模工具可以构成一种有效的方法来分析在单个重复单元 SRU 或堆栈内发生的所有耦合质量和能量传递对性能的影响。

在 SOC /堆叠表中，最近已经开发出具有不同复杂程度的几种模型来研究 HTSE^[31-38]和共电解^[14, 27, 39-46]过程。关于合成气生产，在建模方法中已经考虑了两个主要假设。第一个是基于仅通过反向 WGS 反应产生的 CO^[14, 27, 38]，第二个考虑到二氧化碳电解和 WGS 反应容易产生 CO^[39, 43-45]。在后一种情况下，显示 WGS 反应的相对方向可以取决于入口组成和电化学电池内的位置^[39, 44]。应该注意的是，反向 WGS 对 CO 生产的相对影响可能依赖于电流。在低电流密度下，化学反应的动力学足够快，从而可以准确地忽略通过电化学还原二氧化碳的 CO 产生^[14, 47]。在较高的共电解电流密度下，CO 电化学生产可能变为主要反应^[24]。

在以前的工作中，在 SRU 或堆叠层面开发完整的 2D 内部模型，以模拟 H_2O 电解^[48]和共电解^[44]引入了共电解机理的宏观表征^[43]，经实验验证^[24, 44]。这些研究主要基于在 $T = 800^\circ\text{C}$ 的等温条件下操作的单个 SOC。然而，堆叠环境中的电池热管理是一个关键问题，根据工作电压可能导致非常高的升温或冷却^[48]。这些温度变化伴随电解池的强烈的热梯度会显着影响电解池的反应，。由于电解池层之间的热膨胀不匹配，这些梯度可能引起机械破坏，如分层^[49, 50]和电极^[51]或电解质裂解^[49]。

本工作旨在通过建模方法建立 H_2O 电解和 $\text{H}_2\text{O} + \text{CO}_2$ 共电解操作图。分析模拟以确定优化的实际操作条件。因此，研究了典型代表堆叠平面的 SRU 几何形状。此外，考虑了当地温度对性能的影响，这种方法应为进一步评估高温电解过程的技术相关性提供了有用的见解。实际上，尽管有一些关于等温 HTSE^[52] 或电解经济评估^[9] 的参数研究，但是尚未研究考虑热和电化学现象之间耦合的操作图。

建模方法

蒸汽电解和共电解模型都在其他地方详尽描述^[21, 44, 48]，然而，本节总结主要研究模型假设，并描述所研究的几何形状和材料。

假设和实验验证

全球模型架构由一个集成传输和电化学模块组成，耦合到一个热传感器。热计算在有限元代码 Cast3M^[53] 的框架中，而电化学模块是使用商业软件 Matlab® 实现的。以下部分重点介绍了辅助电解模型，因为其增加了来自额外气体种类的复杂性。然而，如果没有 CO_2 和 CO 进料到电池中，则可以从以下推导出蒸汽的电解模型。

电化学模块

所提出的共电解模型描述了在阴极侧同时发生的蒸汽（5）和二氧化碳（6）的电还原反应的 H_2 和 CO 产生，同时在阳极侧产生氧气（7）。WGS 反应（4）假设发生在阴极材料的孔中。考虑到在高温和大气压下运行的 SOC，碳沉积和甲烷生产被忽略^[24, 41, 54, 55]。



电动力学通过广义的 ButlereVolmer 方程来描述。因此，电池电压 U_{cell} 被分解为等式（8），其分别是标准电位 $U_{i=0}$ ，欧姆损耗和用于激活和浓缩，超电荷和 h_{conc} 的超电势之和。

$$U_{\text{cell}} = U_{i=0} + R_{\text{ohm}}|i| + |\eta_{\text{act}}^{\text{anode}}| + |\eta_{\text{act}}^{\text{cathode}}| + |\eta_{\text{conc}}^{\text{anode}}| + |\eta_{\text{conc}}^{\text{cathode}}| \quad (8)$$

$$|\eta_{\text{act}}| = \frac{RT}{F} \sinh^{-1} \left(\frac{|i|}{2i_0} \right) \quad (9)$$

通过能斯特方程计算表明浓度超电势描述了沿着电池的活性物质耗尽、产生

以及通过多孔电极的扩散而导致的电压增加。考虑电化学动力学的活化超电势取决于交换电流密度 i_0 (等式 (9)), 其表示电极材料进行相应的电化学反应的准备。在目前的宏观尺度建模方法中, 电化学活性区被还原成电极、电解质界面。对于足够厚的电极, 这种假设的相关性已得到很好的验证^[56-58]。因此, 交换电流密度是包括全局电化学过程及其在有源层中的离域的宏观参数^[59]。由于存在二氧化碳, 燃料电极的活性位置不能完全用于水分子电解。因此, 阴极的每个基本活性表面已经分裂成与 H_2O 电解相关的一个表面, b 和与 CO_2 的电化学还原 $1-b$ 有关的第二个表面^[43]。此外, 两种电化学反应的局部活性位点分布被认为是由阴极、电解质界面处的 H_2O 和 CO_2 的相对百分比 (式 (10)) 直接给出的:

$$\beta = y_{H_2O}^{int} / (y_{CO_2}^{int} + y_{H_2O}^{int}) \quad (10)$$

在尘埃气体模型 (DGM) 的框架内描述了多孔电极中的质量传递, 结合了 StephaneMaxwell 和 Knudsen 扩散机理^[61]。它由电化学界面的活性物质的生产和消耗流动驱动。假设理想的电流效率 (即电解质中的离子输送数量等于 1), 这些流量通过法拉第定律与电流密度相关。

散热模块

SOC 的热描述包括传导, 对流和辐射的传热^[48, 62]。由于在两个电极内计算的佩佩克数远低于单位, 多孔阳极和阴极被建模为仅考虑有效传导的均匀介质^[63]。通过固体和流体的外表面之间的对流进行的热传递允许将气体温度变化计算到气体分布通道中。最后, 模型中还考虑了 SRU 和堆叠绝缘之间产生的辐射损失。

电化学和热耦合

在堆叠配置中, 极化下的温度演化可以大大影响性能, 而热梯度可能会影响 SOEC 的结构完整性^[51]。因此, 在本工作中已经特别注意评估局部温度变化对细胞反应的影响。为此, 热模块紧密耦合到电化学模块:

(1) 在电化学模型中计算热源或水槽的产生, 作为化学和电化学动力学的函数。这些源或汇被用作温度计算的热负荷。根据 (i) 重新分解阴极内的 WGS 反应速率和 (ii) 沿着与电解质的界面的电化学反应速率的演变, 它们在电极中空间分布。此外, SRU 内的气体组成分布允许表示在热模块中使用的热流体性质的变化。因此, 通过混合定律计算沿着气体通道的每个位置的流体的有效电导率。阳极和阴极侧的固体和气体之间的热交换系数由有效气体导电率表示。

(2) 相反, 来自热模块的温度场用作电化学模型中的边界条件, 实际上, 根据 Arrhenius 定律, 温度影响电解质的局部离子电导率 (而电极的电导率应该足够高到不依赖于温度)。反映电化学动力学的 WGS 反应的动力学常数和电极交换电流密度也被假定为用于热激活的。因此, 交流电流密度通过 Arrhenius 定

律计算为局部温度 T 的函数（表 1）：

$$i_0(T) = i_0^0 \exp\left(-E_a/RT\right) \quad (11)$$

其中 i 是预指数因子， E_a 是活化能， R 是气体常数， T 是局部温度。最后，可以注意到气态物质的扩散表现出非活化的温度依赖性。实际上，Knudsen 系数在模型中与温度平方根成比例^[64]。

模型验证

通过电池级别 H_2O 电解， CO_2 电解和共电解中获得的实验和模拟等温极化曲线之间的多个比较来验证^[24, 44]。此外，共电解模型显示准确地预测在 OCV 和 $1.75 A cm^{-2}$ 之间操作的单个 SOC 以及 25 个电池堆的出口气体组成^[22]。在用 CH_4 燃料加入的 SOFC 模式中进行与实验数据的进一步比较^[62]，实验数据和模拟数据之间比较预测 SOC 性能和出口气体组成的能力。

代表 SRU /堆栈的模拟条件设计

在这项工作中，通过建立操作图，已经进行了模拟以估计高温电解、共电解过程的技术潜力。为此，研究了一种典型的平面 SRU 几何结构，将 $10 \times 10 \text{ cm}^2$ 的电池集成在逆流配置中（图 1）。值得一提的是，用于仿真的边界条件已经被假设为代表位于完整堆栈中间的重复单元。因此，绝缘条件已被选择用于互连板的下表面和上表面，而在模拟域外围的外边缘可以通过辐射与堆叠绝缘体（温度保持在 $T = 800^\circ C$ ，见表 1）来研究。模拟电池代表阴极支撑电池（CSC）通常比其电解质支持的对应物有更好的性能。用于 HTSE 的大多数经典材料被认为是：Ni-8YSZ 金属陶瓷作为阴极， ZrO_2 以 $8 \text{ mol} \% Y_2O_3$ （8YSZ）作为电解质， $La_{0.8}Sr_{0.2}MnO_3 \pm d-8SZ$ （LSM-8YSZ）作为氧电极。

在模拟中使用的电池特性列于表 1 中。可以注意到，从与用于模拟考虑的材料相同的材料制成的典型电池上获得的 3D 电极重建中提取了微结构性质^[51, 59]。已调整交流电流密度的指数前因子以获得模拟电极的典型值（即，对于 i ， i 和 i_0 分别为 530 ， 356 和 200 mA cm^{-2} ；阳极分别为 $800^\circ C$ ^[44, 59]，参见表 1）。电极、互连结的接触电阻已经达到对应于优化的堆叠和电池的 0.05 U cm^2 的相对低的值。

Table 1 – Geometric and electrochemical inputs used in the simulations. All other numerical values can be found in Refs. [48,59,62].						
Single repeating unit (SRU) and cell						
Dimensions			Microstructure			
Cathode thickness	1000	μm	Tortuosity factor cathode	τ_c	2.8	–
Electrolyte thickness	10	μm	Porosity cathode	ϵ_c	0.43	–
Anode thickness	50	μm	Mean grain diameter cathode	r_c	1.2	μm
Cell total length	118	mm	Tortuosity factor anode	τ_a	4	–
Cell active length	100	mm	Porosity anode	ϵ_a	0.5	–
Interconnect plate thickness	10	mm	Mean grain diameter anode	r_a	1	μm
Gas channel width	1	mm	Furnace temperature	T_s	800	$^{\circ}\text{C}$
Electrochemical and electrical parameters						
$E_{H_2 \rightarrow H_2O}^0$	120 [51]	kJ mol^{-1}	$\frac{p_{H_2}}{p_{O_2}}(800^{\circ}\text{C})$	536 [51]	mA cm^{-2}	
$E_{CO_2 \rightarrow CO}^0$	120 [52]	kJ mol^{-1}	$\frac{p_{CO_2}}{p_{O_2}}(800^{\circ}\text{C})$	356*	mA cm^{-2}	
$E_{H_2O \rightarrow H_2}^0$	190 [51]	kJ mol^{-1}	$\frac{p_{H_2}}{p_{O_2}}(800^{\circ}\text{C})$	200	mA cm^{-2}	
$R_{\text{interconnect}} = 0.05 \Omega \text{ cm}^2$						
$R_p = \frac{p_{H_2} - p_{H_2O}}{v_{\text{cathode}}} \cdot \frac{p_{CO_2} - p_{CO}}{v_{\text{anode}}} = 1.51 [21,44]$						

* $R_0 = \frac{R_{H_2O \rightarrow H_2}}{i_{H_2O \rightarrow H_2}} / \frac{R_{CO_2 \rightarrow CO}}{i_{CO_2 \rightarrow CO}} = 1.51$ [21,44].

考虑用于共电解研究的阴极入口气体组成在表 2 中给出。它被选择为应当导致以 $\text{H}_2/\text{CO}_2=3/1$ 的比率生产合成气。实际上，该比例构成通过化学方法进一步转化为合成甲烷的组成^[6]。

关于 H_2O 电解模拟，入口组成已经达到 90/10 体积%的 $\text{H}_2\text{O}/\text{H}_2$ ，可以注意到，所研究的电解和共电解组合物在入口处含有相同比例的氧化物质。在这种情况下，给定流量和电流密度的全局转换率将是相同的，因此可以直接比较性能。在两种电解模式中，氧电极都被假定为供给空气。如表 2 所示，已经检测了大范围的流量，在共电解模式中为 12 至 48 $\text{NmL} \cdot \text{min}^{-1} \cdot \text{cm}^{-2}$ ，HTSE 模式为 20 至 95 $\text{NmL} \cdot \text{min}^{-1} \cdot \text{cm}^{-2}$ 。

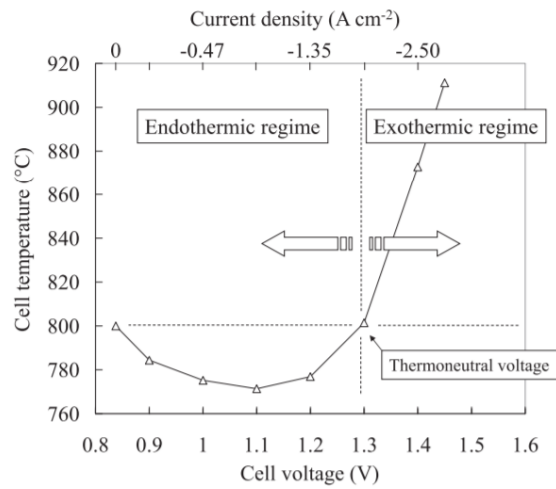


Fig. 2 – Temperature taken in the middle of the cell plotted as a function of the polarization when the SOC is operated in H_2O electrolysis mode (inlet composition corresponding to simulation A1 – Table 2).

结果与讨论

实验验证要素

除了已经出版的模型验证（参见章节假设和实验验证）之外，本实验中计算的性能与在实验室中在相同的进气操作条件下测试的短堆栈获得的性能相比是有利的温度。

基于表 1 收集的假设、参数，模拟评估在 1.2V（阴极流量：15 $\text{NmL} \cdot \text{min}^{-1} \cdot \text{cm}^{-2}$ ）的 90/10vol% H_2O 、 H_2 下的电流密度为约 0.8 Acm^{-2} ，800 $^{\circ}\text{C}$ 的温度用作边界条件）。在类似的操作条件下，在 CSC Ni-YSZ / YSZ / LSCF-YDC 3 电池堆上测量了 1.2V 下的 1A 电流，其活性面积为 100 cm^2 / cell（90/10 体积% H_2O / H_2 ，15 $\text{NmL} \cdot \text{min}^{-1} \cdot \text{cm}^{-2}$ ，气体预热至 800 $^{\circ}\text{C}$ ，堆叠绝缘体调节至 800 $^{\circ}\text{C}$ ）^[66, 67]。值得深刻的是，模拟和实验之间的目前比较仅仅是指示性的，因为这两种方法都不考虑相同的单元格。因此，实验电流密度和模拟电流密度之间的微小差异可能由空气

电极材料的差异引起，与 LSM 相比，LSCF 通常表现出更高的活性（即更高的交换电流密度）。

温度对性能的影响

在 H_2O 电解中研究了极化对叠层热和电化学响应的影响（对于组成 A1，表 2）。如图 2 所示，SRU 中央部分的温度作为电池电压的函数作图。在 OCV 中，由于没有电流流过 SRU，所以温度等于作为边界条件（即对应于进气口和堆叠绝缘温度的 $T = 800^\circ C$ ）的温度。然而，当极化增加时，通过三种热模式证明强烈的演变：吸热，自热和放热模式。当电池电压等于热中性电压（即，对于 H_2O 电解在 $T = 800^\circ C$ 下为 1.29V）时，所提供的电功率能够精确地平衡蒸汽解离的焓（对应于吸热反应（5））。在这种情况下，没有升温或冷却，所得到的堆叠温度等于 $800^\circ C$ 。对于低于热中性电压的偏振，由于电能完全不考虑电化学反应的要求，所以能隙必须由外部供热提供。因此，电池以吸热模式工作，温度降低到 $800^\circ C$ 以下（图 2）。对于高于热中性电压的极化，产生额外的热量，平均电池温度升高超过 $T = 800^\circ C$ 。在所选择的条件下，在 1.45V 下，发现电池的平均温度超过 $900^\circ C$ 。这种非常高的温度构成了将在下一节讨论电解槽退化的条件。

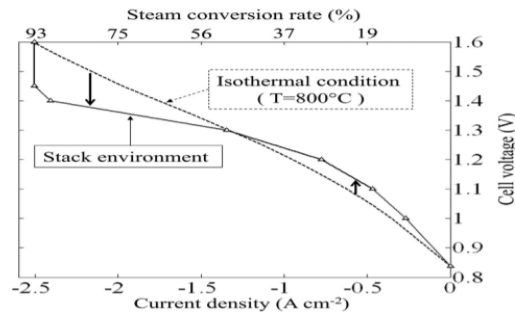


Fig. 3 – Influence of the temperature on performances (H_2O electrolysis, conditions A1). Comparison between the polarization curve obtained for the stack and the one simulated with isothermal operating condition.

这些由堆叠热方式引起的温度变化易于对电池性能产生显著影响。为了对这些潜在影响给出一些解释，考虑到堆热边界条件计算出的极化曲线与用等温假设获得的极化曲线进行了比较。这最后一个条件通常代表特征在测试台中的纽扣电池（在这种情况下，通过炉施加的受控温度来缓解电池升温或冷却）。两种情况之间的比较如图 1 所示。在吸热模式下，发现用堆叠环境计算的电流密度低于等温条件下的电流密度。相反，高于热中性电压（即放热操作），电池性能得到提高。例如，在 1.4V 时，电池电流密度在等温条件下从 $1.7 A cm^{-2}$ 上升到堆叠环境中的 $2.4 A cm^{-2}$ 。两个曲线之间的差异与热激活现象有关^[68]。实际上，电解质的离子电导率很大程度上取决于温度（对于 8YSZ，从 800 到 $850^\circ C$ 为 +51%^[68]），使得任何温度升高降低了欧姆损耗，从而增加了电池性能。然而，这里研究的 CSC 配置

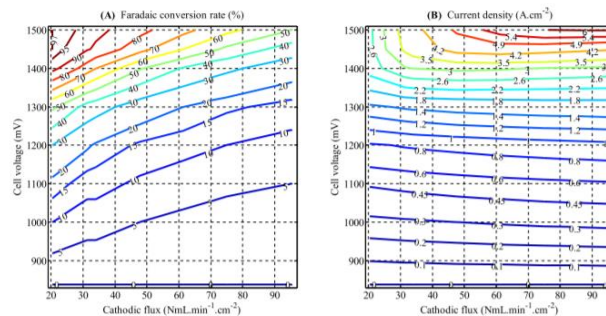
显示了薄的电解质层，其对整体超电势的贡献是有限的。因此，当温度升高时，温度对性能的影响主要由较高的交流电流密度来解释。实际上，活化能相对较高（表 1），因此任何温度升高都会导致 i_0 增加，降低相应的激活超电位（等式(9)）。

最后，值得注意的是，温度升高对电池极限电流密度没有显著影响，如图 1 所示。实际上，极限电流分配给浓度超电势。因此与活性位点有关，导致 (i) 通过电极扩散的质量传递限制和 (ii) 由于蒸汽转化率引起的热力学损失。如已经提到的，前一种扩散过程的温度依赖性相当弱，而后者也非常轻微地取决于温度。值得注意的是，陡峭的几乎垂直的极限电流在实验上证明^[24]，转换率几乎与图 1 中所示的相同。

温度对电解性能的影响进行了类似的观察。然而，OCV 下的电池温度仅为约 797.5°C（即，比气体入口和绝缘外壳的温度小 2.5°C）。实际上，所研究的入口阴极组成是接近的，但不符合在 $T = 800^\circ\text{C}$ 时 WGS 反应的热力学平衡。结果是，由于化学反应引起的散热器对电池温度和在 OCV 下沿着电池的气体组成。通过改变入口组成可以预见更显著的影响。此外，由于二氧化碳电解和 WGS 反应，与 H_2O 电解相比，热中性电压发生变化。在当前的模拟条件下，发现热中性电压约为 1.32V。在这种情况下，发现模拟电池温度等于炉温，如预期^[41]，该值包括对应于纯蒸汽电解（1.29V）的下限和在 800°C 下由纯二氧化碳电解（1.46V）给出的上限。

H₂O 电解操作图

蒸汽转化率，电流密度， H_2 生产和电解池长度中间采取的温度的 H_2O 电解操作图如图 1 所示。模型的这些输出参数绘制为电池电压和阴极流量的函数。



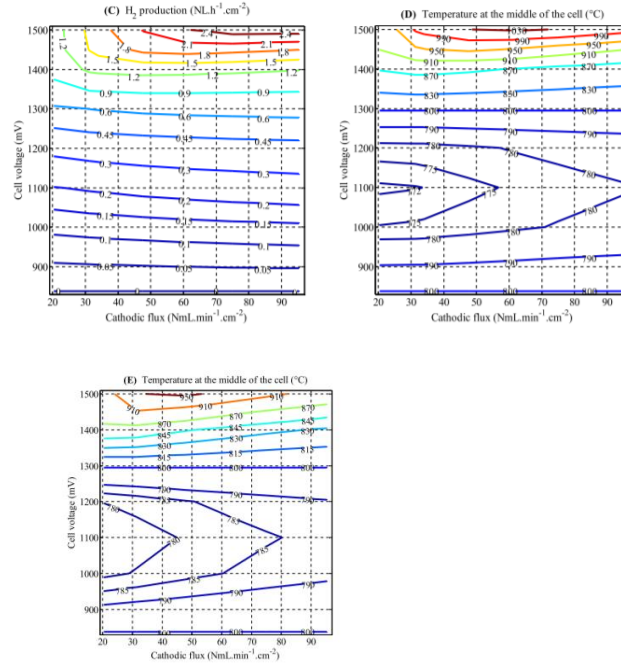


Fig. 4 – H₂O electrolysis operating maps: (A) conversion rate, (B) current density, (C) H₂ production, (D) temperature calculated at the middle of the cell length (input data given in Tables 1 and 2). Cartography (E) corresponds to the temperature at the middle of the cell when the anodic air flow rate is multiplied by three (the other input parameters remaining unchanged).

模拟的操作条件（表 2）可以产生大范围的蒸汽转化率，从 0 到约 97%（图 4-A）。在给定的流速下，增加电池电压，从而提高电流密度，提高蒸汽法拉第转换速率（图 4-A）。此外，无论电池电压如何，较高的阴极通量产生较低的转化率。例如，当气体通量增加 2.2 倍时，1.3V 的转化率从 40%降低到 20%，从 28.5 降低到 61.3 NmL · min⁻¹ · cm⁻²。

再次假设没有气体泄漏和理想的电流效率，通过法拉第定律，H₂的产生与电流密度成正比。因此，4-B 和 C 只有比例因子的不同。由于在低和中等超电势下可以注意到，电流密度和蒸汽转化几乎不受阴极入口流速的影响。尽管如此，由于浓度过低，电流密度稍高，流量更高。相反，在高超电势的情况下，发现通过增加流速来强化电流密度。实际上，在这种极化状态下，浓度超电势足够大以至于在其它电池损耗中变得普遍。在这种条件下，在极限电流下获得的最高蒸汽转化率达到最低研究阴极流速。

在本研究的范围内，发现吸热操作中电解池的冷却是合理的。实际上，在 20 NmL · min⁻¹ · cm⁻²的流速下获得的最冷温度为 770°C。在这些条件下，热现象对电解槽全局响应的影响有限。然而，在放热操作模式下，电池电压高于 1.35 V 时，温度超过 850°C。值得注意的是，应避免这种极端温度升高以保持堆叠完整性。事实上，这些高温绝对会通过加速所有热活化的降解过程如 Ni 附聚，电池组分之间的材料反应性等而对材料的稳定性造成不利影响^[68]。此外，电池温度的水平强烈依赖于系统设计和指定的边界条件。在本工作中，假设堆叠可以通过辐射与热调节的绝缘外壳交换热量。这种情况导致在放热操作模式下缓冲电池升温（因

为部分散热可被绝缘体吸收)。对于没有热调节的系统设计,所产生的热量只能被气体流除去,使得温度上升将变得更陡峭。因此,温度升高如图 1 所示。2 可以被认为是不同系统设计的下限。

为了减轻堆高度而不影响性能,一个解决方案可能包括增加阳极侧的空气吹扫。为了研究这种可能性,在将阳极侧的流量增加三倍(所有其它输入模型参数保持不变)之后,进行了仿真,如图 1 所示。如图 4-E 所示,在阳极侧的改进的对流热交换允许在放热的操作模式中显着降低温度。因此,这种方法似乎是一种有趣的方法,尽可能地将堆叠操作扩展到热中性点电压以上。

无论缓解方案如何,堆叠必须在安全的工作条件下运行,以保持低于 850°C 的合理温度^[68],关于图 1 所示的操作图。4-D 或 E,这导致将电池极化限制在 1.35V 以下。此外,对于电解槽来说,经济上可行,蒸汽转化率应保持在 50% 以上^[69]。这两个主要因素决定了 H_2O 电解的最佳工作条件: $1.29 < U_{\text{cell}} < 1.35 \text{ V}$, $20 < F_{\text{cathode}} < 40 \text{ NmL/min/cm}^2$ 。

在最佳操作条件的这种范围内,每单元活性面积为 100cm^2 ,在 1.3V 和 $20 \text{ NmL} \cdot \text{min}^{-1} \cdot \text{cm}^{-2}$ 下操作的 25 个电池堆将产生 1.4Acm^2 的电流密度,50% 的转化率和 H_2 生产率 $1.5 \text{ Nm}^3 \text{ h}^{-1}$ 。在这些条件下,计算出的电解槽温度约为 800°C ,从而简化堆热管理。定义为所生产的氢气中所含的能量与消耗的电力之间的比率的电效率达到 96% (注意,电效率的定义仅与自由和可用的热源相关)。相比之下,碱性和 PEM 电解槽的电效率分别为 62% 和 68%^[68]。然而,可以指出, SOC 耐久性达到相当高的电流密度为 1.4Acm^2 , 仍然有待检查。如果对于这种操作条件,降解速率变得太高,则一个解决方案可能是将入口流速降低到低于 $20 \text{ NmL} \cdot \text{min}^{-1} \cdot \text{cm}^{-2}$ 。在 1.3V 时,转换率将高于 50%,电效率将严格保持不变为 96% (不依赖于电流)。然而,在这种情况下,每堆的氢生产率将降低。

电解电解操作图

图 1 给出了电流密度,转化率,合成气生产和温度的电解电解操作图。可以注意到,所调查的参数集合(表 2)导致了 0-96% 的转换率范围。与 H_2O 电解模式类似,在给定的电池电压下,增加阴极通量产生略高的电流密度(图 5-A)。再次,这是由于较低的浓度超电势,因为获得较低的转化率(图 5-B)。尽管有轻微的增加,电流密度被认为是全局稳定的,作为入口流量的函数,特别是当 $F_{\text{cathode}} > 20 \text{ NmL} \cdot \text{min}^{-1} \cdot \text{cm}^{-2}$ 时。因此,得到的电池温度(图 5-D)仅略微取决于入口流量。实际上, H_2O 和 CO_2 的解离焓是可比的,绝对值大大优于 WGS 反应的焓。共同电解电流密度与其相应的电池电压因此控制发热,并且如上所述,在本研究的参数范围内是稳定的。此外,合成气 H_2CO_3 生产曲线也遵循电流密度(图

5-C)，并且与 WGS 反应速率无关。事实上，这种化学反应是等摩尔的，并且消耗一分子的 CO 以产生 H_2 中的一种（反之亦然）。在这种情况下，WGS 反应不能改变所产生的合成气的总通量，即使它可以影响其组成。

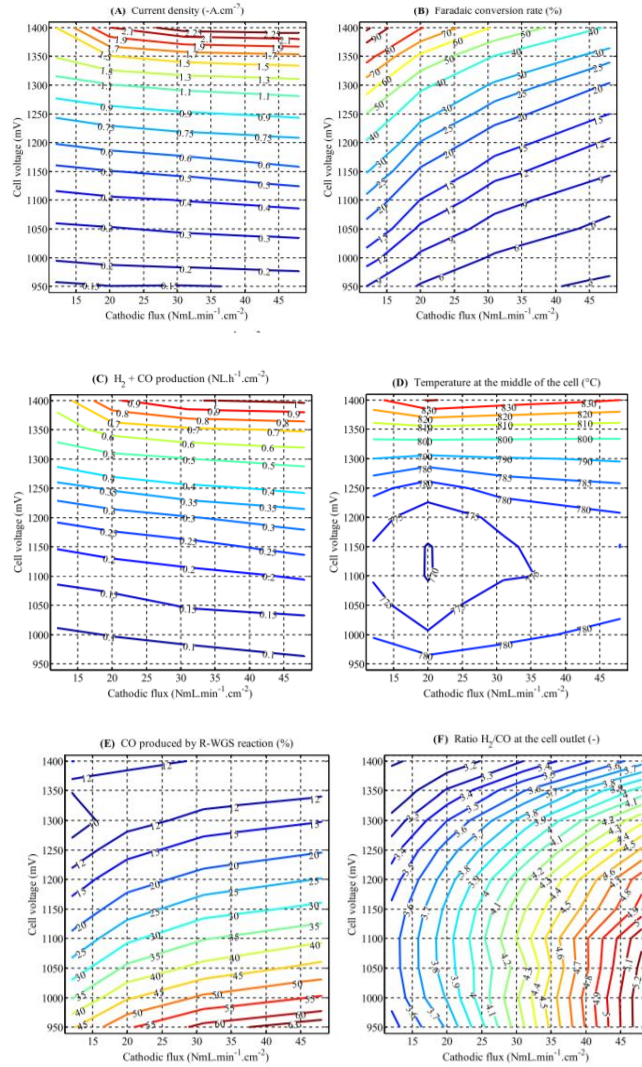


Fig. 5 – Co-electrolysis operating maps: (A) current density, (B) conversion rate, (C) syngas production, (D) temperature taken at the middle of the cell length, (E) CO produced by the reverse WGS reaction, (F) H_2/CO at the cell outlet.

通过化学反应（5）在全球（即化学和电化学）生产中产生的一氧化碳的相对比例，5-E 呈现了 WGS 反应对共电解过程的全球影响。因此，在全球消耗 CO 的化学反应的情况下，值可以是负的。在图 5- E 中，仅计算正值，在“反向”方向全局支持 WGS 反应。可以注意到，这并不一定意味着 WGS 反应在厚阴极衬底内的任何地方都以相反的方向工作^[21, 44]。如先前低入口流量所证明的那样，反向 WGS 反应产生的 CO 的量随阴极流速（即较低的转化率）而增加，而其贡献是电池电压的递减函数。例如，即使通过将阴极流速提高到 $48 \text{ NmLmin}^{-1} \text{ cm}^{-2}$ ，发现只有四分之一的产生的 CO 来源于 1.2V 的反向 WGS 反应。以前的工作中更详细地讨论了二氧化碳电解对 CO 生产对 WGS 反应的普遍性^[24]。然而，由于反向 WGS 反应的贡献绝对不能忽略，因此，电池出口处的 H_2/CO 比取决于操作条件（即入口流

速和组成，温度，电池电压等），如图 3 所示。

这些操作图可用于确定关于完整的电力-燃料过程的最佳操作条件。鉴于上述结果，最小可接受的转化率可能是共同电解操作最相关的参数。此外，当使用镍基金属陶瓷时，可以避免非常高的电流密度（即 $> j-2jAcm^{-2}$ ），因为显示它可能导致碳沉积^[70,71]。因此，在调查范围内，人们可以认为，在 1.35 V 时，20 $NmL \cdot min^{-1} \cdot cm^{-2}$ 可能是实际操作的中间位置，产生 1.5 Acm^2 和 60% 的转化率。然后，该共电解器将在稍微放热的模式下在约 810°C 下操作。因此，这仅会稍微降低电池效率，而额外的热量可以允许预热入口气体。使用这些值，25 电池堆共同电解槽的全局输出将对应于 5 kW 的电力，并将产生 1.63 Nm^3h^{-1} 的合成气， H_2 / CO 出口比为 3.3。

H₂O 电解与电解的比较

比较 H_2O 和 H_2O+CO_2 电解操作图显示了几个显着的差异。首先，在入口流量和电池电压相同的条件下，共电解中达到的电流密度低于蒸汽电解中获得的电流密度。与实验报告一致^[13,24]，在给定的流量和电池电压下， H_2O 电解显示出更高的性能和更高的转化率。当接近所研究的最高超电位时，这种差异变得特别显著。这是由于多孔阴极中的多组分（ H_2 ， H_2O ， CO 和 CO_2 ）扩散引起的更严重的质量传输限制。相反，在纯蒸汽电解下， H_2O 和 H_2 的扩散限制较小，从而达到更高的电流密度，导致较高的 SRU 温度升高，反过来又增加了电动力学。这种差异可能构成共电解过程的总体局限性，特别是当阴极微结构未被精心优化时。

然而，在共电解模式下获得的全球较低的电流密度可能对 SRU / 堆热管理产生积极的影响。事实上，与 800°C（图 5-D）相比，在共电解中获得的最高温度升高限于 +40°C，这显著小于 H_2O 电解（图 4-D）。鉴于以前讨论的电流密度对温度的影响，当 $F = 20 NmL \cdot min^{-1} \cdot cm^{-2}$ 时，两种电解模式可以更详细地进行比较。实际上，在这种进料条件下， H_2O 电解和辅助电解模式中的电流密度与电池电压大致相同。图 6 示出了在条件 A1 和 B2 中获得的计算的纵向温度曲线（表 2）。可以看出，与 H_2O 电解操作相比，共电解模式中的温度升高和梯度显著降低。例如，在 1.4V 时，中间电池的温度约为 840 和 860°C，而最高和最冷的局部温度之间的差异分别在共电解和 H_2O 电解模式中约为 5 和 20°C。

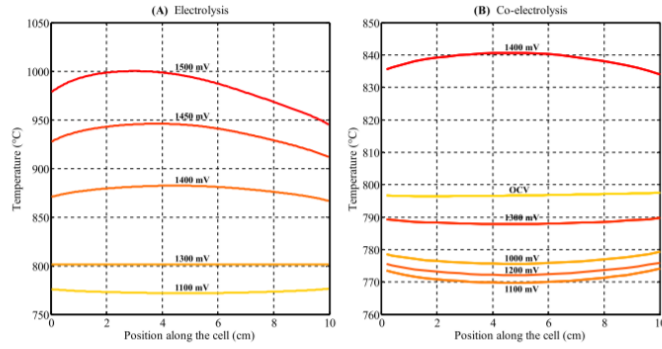


Fig. 6 – Longitudinal evolutions of cell temperature as a function of the cell voltage when the cell is fed with (A) 20 NmL min⁻¹ cm⁻² of 90/10 vol.% H₂O/H₂ and (B) 65/25/10 vol.% H₂O/CO₂/H₂.

电解池温度和热分布的这种差异可以通过几个因素来解释。首先，如前所述，共电解中的热中性电压取决于入口气体组成，并且与蒸汽电解相比，其转移到更高的电压。考虑到入口组成 65/25/10 体积% H₂O / CO₂ / H₂，这里评估为约 1.32V。这意味着放热模式中任何给定的操作电池电压将更接近于辅助电解模式中的热中性电压比 H₂O 电解。这种现象包括轻微吸热反向 WGS 反应，在模拟条件下有利（图 5-E）。此外，在电解操作中阴极气体混合物的体积热容增加。实际上，CO 和 CO₂ 分别比 H₂ 和 H₂O 分别显示出更大的 Cp（33.7 和 55.4 Jmol⁻¹K⁻¹ [72]）（30.3 和 42.4 Jmol⁻¹K⁻¹ [72]）。因此，阴极气体流在电解过程中能够排出比在 H₂O 电解中更多的热量，对温度和热梯度有积极的影响。

除了辅助电解直接生产合成气的明显优势外，与蒸汽电解相比，这些结果表明，与堆叠环境相比尤其重要，热管理更容易。因此，与 H₂O 电解相比，共电解可以表现出更宽范围的可接受的操作条件，因为高热梯度已显示引起机械应力，可能导致电池故障^[51]。根据实验观察^[13, 24]，发现在类似条件下，电解性能低于 H₂O 电解。因此，与电解相比，在电解中的热中性电压以上的温度升高被发现是更显著的。此外，发现纵向热梯度在 H₂O 电解中更陡峭，导致可能更严格的机械应力和材料降解速率。在计算的共电解极化曲线的放热部分中，可能产生较高电流密度的较高温度的益处受到强大的质量传输限制的阻碍。实际上，模拟了最大电流密度，导致当阴极流速增加时转化率大幅下降。因此，致力于电解池支持的微观结构优化研究以提高 CO / CO₂ 气体输送的研究应该是提高电解操作中电解池效率有希望的途径。

此外，在完整的模拟中，发现 CO₂ 电还原占 CO 生产的大部分，因为反向 WGS 反应产生的 CO 仅在 1.3V 的 10-15% 范围内。此外，出口比 H₂/CO 显示取决于电流密度、入口阴极流速和温度。鉴于与特定的后电解器方法（例如甲烷化反应）的耦合，这些参数都可以是可调整的变量以获得特定的出口气体组成。